Pore accessibility and trapping of methane in Marcellus shale

Andrzej P. Radlinski[a], Tomasz Blach[a], Phung Vu[a], Yeping Ji[a], Liliana de Campo[b], Elliot P. Gilbert[b], Klaus Regenauer-Lieb[a,c] and Maria Mastalerz[d]

[a]School of Minerals and Energy Resources Engineering, Kensington, University of New South Wales, Sydney, NSW 2052, Australia
[b]Australian Centre for Neutron Scattering, Australian Nuclear Science and Technology Organisation, New Illawarra Road, Lucas Heights, NSW 2232, Australia
[c]WA School of Mines: Minerals, Energy and Chemical Engineering, Curtin University, Bentley 6102, WA, Australia
[d]Indiana Geological and Water Survey, Indiana University, Bloomington, IN 47405-2208, USA

Abstract

Accessibility of pore space in unconventional reservoirs is an important factor influencing both methane storage capacity and the kinetics of methane desorption. The determination of open (accessible) versus closed (inaccessible) porosity is therefore vital for the prediction of gas production potential. This study investigates accessibility of pores to methane in overmature middle Devonian Marcellus shale samples (cut parallel and perpendicular to bedding) using small and ultra-small neutron scattering (SANS and USANS) with contrast matching (CM), supplemented by other complementary techniques, such as mercury injection capillary pressure (MICP) and low pressure gas (N_2 and CO_2) adsorption.

Our results demonstrate that for the samples studied, only about 6 % of pores with diameter 25-500 nm are accessible to methane. The accessibility fraction for pores larger than 500 nm is 35%. For nanopores smaller than 25 nm, pore accessibility could not be quantitatively determined due to increased methane density and condensation effects in confinement. Our observations indicate that methane penetrates the accessible small mesopores and micropores down to at least 1 nm in diameter, and the density of confined deuterated methane (CD_4) is 0.68 g/cm^3 for pores of diameter 25 nm and gradually increases with the decreased pore size. Morover, elevated gas pressure causes formation of additional high-density methane nano-clusters. These clusters have a form of slightly anisotropic polydisperse discs oriented along bedding plane, about 1-12 nm in diameter and with average thickness of 3.6 nm. Utilizing samples cut parallel and perpendicular to the bedding, this study also briefly addresses anisotropy of pores. Based on the iso-size intensity ratio $\mathscr{R}$, our SANS and USANS results demonstrate anisotropy in the out-of-bedding direction and suggest that the degree of anisotropy depends on the pore size. Specifically, for pore diameters ~2.5 to 250 nm, the

extent of anisotropy is smaller than for pores ~500 nm to 6 μm in diameter. Finally, comparison of pore size distribution results calculated from SANS/USANS to those obtained using MICP shows good agreement at low pressures, but large difference at pressures above 1000 bar. This discrepancy requires further testing; it is possible that the high mercury pressure used in MICP alters the mesopore and micropore structure of shales.

Keywords: pores, methane trapping, shales, neutron scattering, Marcellus shale

1. Introduction

More than 60% of the natural gas in the USA currently comes from unconventional shale reservoirs, and it is predicted that these reservoirs will account for 75% by year 2050 (US EIA, 2020). Even though contribution of other energy sources such as wind or solar power or geothermal energy to the energy portfolio continually increases, natural gas from unconventional reservoirs will undoubtedly be an important energy source, not only in the USA, but also in many other countries for years to come. This increasing contribution from unconventional shale reservoirs was possible due to advances in horizontal drilling and hydraulic fracturing that allowed tapping into vast new resources of gas (Elsaig et al., 2016). However, unconventional gas recovery is not free of technological, economic and environmental challenges, and with low recovery rate is one of the main issues (Lee et al., 2011: Cao et al., 2017). Due to the low porosity and permeability of shales (e.g., Jarvie et al., 2007), gas recovery rates using current hydraulic fracturing methods are still no greater than 20% (Dong et al., 2013; Lijun et al., 2017). Consequently, the majority of natural gas remains trapped in the reservoir. Improving the efficiency of unconventional gas recovery would be a major breakthrough for energy economics.

Several studies have suggested that the accessibility of pore space in unconventional reservoirs (coal and shale) is an important factor influencing both methane storage capacity as well as methane desorption, and that quantifying open (accessible) versus closed (inaccessible) porosity is vital for predicting gas production potential. Closed pores are important because they may contain methane, and the ability to access these pores will potentially influence the gas recovery (Wang et al., 2018). Open pores, in turn, form transport pathways for the gas and they are responsible for fluid flow in the rock matrix (Zhang et al., 2020). Based on a negative correlation between pore accessibility and the maximum gas adsorption, Wang et al. (2018) suggest that there may be an optimal value of pore accessibility in shales that will maximize gas production; thus, determination of these values for prospective shales may help to plan and direct drilling programs. They conclude that shale reservoirs with relatively high pore accessibility will quickly produce significant amounts of gas at relatively low threshold pressures. In turn, there could be a gradual sustainable methane production from low pore accessibility shales even though the initial amounts of produced gas may not be large. Another important consideration is that proportions of open to closed porosity will change with change in temperature and pressure (Melnichenko et al., 2012). Consequently, if pore accessiblity is known, and its changes with reservoir and production conditions could be realistically predicted, the production well management and hydraulic fracturing operations could be adjusted to control the percentage of accessible pores to optimize gas volumes over various production phases.

Determining accessible versus inaccessible porosity in shale is challenging because commonly used adsorption porosimetry techniques (He pycnometry, low pressure N_2 or CO_2 adsorption or mercury injection capillary pressure - MICP) are not able to provide information about closed pores (Chalmers et al., 2012; Wang et al., 2016). In turn, neutron scattering techniques (small-angle neutron scattering, SANS, and ultra-small-angle neutron scattering, USANS) that record the scattering intensity from all pores, can be used to characterize closed plus open pores within the detectable size range. Consequently, to obtain closed porosity, some studies combine neutron scattering techniques and adsorption techniques (e.g., He pycnometry) to subtract open porosity from the total porosity (e.g., Clarkson et al., 2013; Wang et al., 2018). However, because data from different techniques are not easy to compare and rely on different uderlying assumptions, the closed porosity values obtained this way should be treated with caution. Recent developments in SANS and USANS methods enable the discrimination between open and closed porosity by using contrast matching (Melnichenko et al., 2012; Bahadur et al., 2016; Blach et al., 2018). In this technique, the density of the pore-invading fluid (CD_4 or heavy water, D_2O) is varied to match the scattering length density (SLD) of the solid matrix (e.g., coal or shale). When the SLD of the fluid matches that of the solid matrix (the full contrast matching condition), the scattering from all pores accessible to the fluid is eliminated and the remaining scattering comes only from the pores inaccessible (closed) to the fluid.

This work addresses accessibilty of pores to methane in samples of Middle Devonian Marcellus Shale, a gas-producing formation comprising the largest natural gas field in the United States (Lee et al., 2011). Previous studies using the CM SANS technique have been performed on Marcellus Shale samples from different depths at several geographical locations and indicate a significant variation of deuterated methane accessibility (F_a) and density (d) in nanopore confinement; nanopores are defined here as having diameters in the range from ~1 nm to ~100 nm, with the sub-class of the narrowest pores (2r < 10 nm) previously referred to as SDN (Single Digit Nanopores; Faucher et al., 2019). Specifically, for the 1-5 nm nanopores of a sample from the northern Appalachian Basin (depth 2599 m; reflectance of vitrinite, R_o, equal to 3.3%; porosity, Φ, equal to 6%), Eberle et al. (2016) reported methane densification by a factor 2.1±02 at T = 21±0.4 ºC. In turn, Jubb et al. (2020) studied samples from West Virginia (depth 2307 m and 2310 m, H/C atomic ratio ~0.45) at T = 60ºC (estimated reservoir temperature) and determined that (i) ~75 % of the 25 nm diameter pores were accessible to methane, and (ii) pore accessibility decreased for smaller pores (we also note that densification is evident from their experimental data for pores smaller than 1.5 nm in the 2307 m sample). In addition, for samples from West Virginia (depth 2299.46 - 2300.26 m) measured at room temperature at CD_4 pressures between 310 and 414 bar, Neil et al. (2021) reported kerogen swelling related to the formation of pressure-induced sub-4 nm diameter clusters of CD_4.

In this study, the CM SANS and CM USANS techniques are used to provide more information about the micro- and nanostructural characteristics of the accessible and inaccessible pore space in Marcellus Shale. In particular, the interpretation of SANS data is scrutinized in detail and compared with the MICP and gas adsorption results in the nanopore region. In our early work on CM SANS (Melnichenko et al., 2012), we introduced the term ZAC (Zero Average Contrast) to describe the full contrast matching condition, which subsequently became accepted in geoscientific SANS and USANS research. The term ZAC, however, has been long before used in polymer science to describe a different physical phenomenon (Benmouma and Hammouda, 1997; Gilbert et al, 2001). To avoid possible future confusion, in this paper we use the term CM (Contrast Matching) rather than ZAC.

2. Background of small angle neutron scattering

Theoretical foundations of SANS and USANS relevant to scattering from shales are discussed by Radlinski (2006), Anovitz and Cole (2015), Melnichenko (2016) and Zhang and Chang (2021).

Scattering of neutrons occurs effectively at the interface between various physical regions of the rock and is caused by the non-zero scattering contrast, $(\Delta\rho)^2 = (\rho_1 - \rho_2)^2$. The symbol ρ_i represents the scattering length density of each uniform region (phase) of the rock (used interchangeably with the acronym SLD), and can be calculated if the isotopic chemical composition and matrix density are known (e.g. Radlinski et al., 1996; Radlinski, 2006; NIST calculator - https://www.ncnr.nist.gov/resources/activation). For shales, the most abundant mineral components of the rock matrix have similar SLD values that, in addition, are only slightly different from the SLD of the over-mature organic matter (Radlinski, 2006; Thomas et al., 2014). This is particularly valid for the studied sample Marcellus_7084, where the measured SLD of the shale and calculated SLD of the organic matter agree within experimental error (section A2 of the Appendix). The scattering intensity per unit volume, I(Q) (where Q is the scattering vector), is then dominated by the contrast (or, specifically, the square thereof) between the two supra-phases: the solid rock matrix and the content of pores. Debye et al. (1957) have shown that in the two-phase approximation I(Q) has the form:

$$I(Q) = \{4\pi(\Delta\rho)^2\Phi(1-\Phi)\}\int_0^\infty r^2\gamma(r)\frac{\sin(Qr)}{Qr}\,dr = (\Delta\rho)^2\Phi(1-\Phi)F(Q) \quad (1)$$

where $Q = (4\pi \sin\theta)/\lambda$ is the scattering vector, 2θ is the scattering angle and λ is the neutron wavelength. F(Q) is called the form factor, $\Delta\rho = (\rho_m - \rho_g) \equiv$ [*SLD(rock matrix)* - *SLD(pore content)*], Φ is the total porosity of rock, and $\gamma(r)$ is the density-density correlation function. The scattering intensity for shales can often be approximated by a sum of a power law and a (small) background scattering:

$$I(Q) = A \cdot Q^{-n} + B \quad (2)$$

where A is the power-law prefactor, B is the so-called "large-Q background" and n is the power exponent which takes values of $1 \leq n \leq 4$. This form corresponds to the scattering from fractals (e.g. Radlinski, 2006). As the Q-value decreases, n may decrease from $3 < n < 4$ (surface fractal scattering characterised by fractal dimension D_s, where $n=6-D_s$) to $2 \leq n \leq 3$ (three-dimensional mass fractal scattering, where $n=D_m$) (Wong and Lin, 2006; Anovitz and Cole, 2015; Anitas, 2017). The transition usually occurs near the value of $Q = Q_0$, corresponding to the correlation length (grain size) of the order of $1/Q_0$. Scattering by fractals is mathematically equivalent to scattering from a polydisperse distribution of pores (Pfeifer and Avnir,1983; Schmidt 1982):

$$N(r)\,dr = N_0\, r^{-(1+D_s)} \cdot dr \quad (3a)$$

For an arbitrary polydisperse pore size distribution:

$$N(r)\,dr = N_0\, f(r)\,dr \quad (3b)$$

where f(r) is the probability density of pore radius r (pore diameter is equal to 2r) and N_0 is the total concentration of pores. For any polydisperse distribution of spherical pores, including the fractal one, Equation (1) becomes (Espinat, 1990; Liu and Zhang, 2020):

$$I(Q) = (\Delta\rho)^2\int_0^\infty N(r)\,[v(r)]^2\,F_0(Q,r)dr \quad (4a)$$

or, alternatively,

$$I(Q) = (\Delta\rho)^2 N_0 \int_0^\infty f(r)\,[v(r)]^2\, F_0(Q,r)dr \qquad (4a)$$

where N(r) is the number of spheres within the radius interval (r, r+dr) per unit volume (i.e. the number density of pores or concentration of pores of this size, measured in cm^{-3}), v(r) (= $4\pi r^3/3$) is the pore volume, and $F_0(Q,r)$ is the form factor for a sphere of radius r, i.e. F(Q,r), normalised to unity at Q = 0:

$$F(Q) = v(r)\ \{[\sin(Qr) - Qr\cos(Qr)] / (Qr)^3\}^2 \qquad (5)$$

Equations 4a and 4b provide an alternative formulation of the Polydisperse Spheres (PDSP) model used in this work, coded in the PRINSAS software (Hinde, 2004). PRINSAS fits a distribution of N(r) in Eq. 4a to the measured absolute values of I(Q) (i.e. in the units of cm^{-1}) and calculates microstructural parameters as a function of r, r^2 and r^3: probability density of pore size, f(r), internal specific surface area versus the molecular probe size, SSA(r_p), differential pore volume distribution ((dV/dr)(r)), and the total porosity (ϕ). The model works well for any broad distribution of pore sizes (not necessarily fractal); it also provides approximate apparent values of microstructural parameters for moderately anisotropic samples (Radlinski et al., 2004b; Gu and Mildner, 2018).

Importantly, for rocks scattering according to the power law an approximate relationship holds:

$$r \approx 2.5/Q \qquad (6)$$

where 2r is the diameter of pores that contribute most of the scattering intensity I(Q) (Radlinski et al., 2000; Melnichenko et al., 2012). According to Eq. 4a this provides an approximate, model-independent linear relationship between I(Q) and the concentration of pores of the size 2.5/Q; I(Q) and N(r) are proportional to each other, even though the functional form of I(Q) for spherical objects extends over a wide range of Q-values (see, e.g. Espinat, 1990).

The scattering intensity in Eq. 1 can be affected by varying the contrast $(\Delta\rho)^2$. In contrast matching (CM) experiments this is done by filling accessible pores either with a liquid or pressurised gas such that SLD(rock_matrix) = SLD(pore_content). According to Eq. 4a, this is equivalent to modyfing the apparent pore number distribution: at the match point, $N(r) = N_i(r)$, where $N_i(r)$ is the number density of inaccessible pores, and, consequently, the total concentration of observable pores becomes equal to the concentration of inaccessible pores, $N_0 = N_{0i}$.

3. Experimental methods

3.1 Samples

This study uses samples of Devonian Marcellus Shale collected from a borehole at a depth of 2159.2 m (7084 feet) in Pennsylvania. Gas production from this formation occurs at depths between 1371.6 m to 2590.8 m (4500 to 8500 feet, Elsaig et al., 2016), the shale used in this study may therefore be considered a "typical" producing horizon. The core fragment (diameter ~50 mm, length ~80 mm) was a megascopically homogeneous black shale (massive texture without visible lamination) of the dry gas window maturity, as indicated by vitrinite reflectance $R_o \approx 2.5$ %. The shale has matrix density of 2.55 g/cm^3, helium porosity of 6.88 % and permeability of $1.6\text{x}10^{-4}$ mdarcy, determined by helium densitometry and pressure decay methods, respectively. Mineralogy, determined by XRD, is dominated by carbonates (37 wt%), quartz (30.6 wt%) and clays (15.5 wt %) (Table 1). Total organic carbon (TOC) accounts for 3.4 wt % and comprises of high maturity solid bitumen (pyrobitumen) and less frequent zooclasts.

Table 1. Mineralogical composition (in wt %, determined using XRD) and TOC value (in wt %, determined by a LECO elemental analyzer SC832DR) for the Marcellus core.

Quartz	Plagioclase	Carbonates	Pyrite + marcasite	Clays	TOC
30.6	5.2	37	8.3	15.5	3.4

In preparation for various analyses, the core was split into two parts perpendicular to bedding. One part provided sub-samples for neutron scattering experiments and the other one was used for the X-ray diffraction (XRD), total organic carbon (TOC) and mercury intrusion capillary pressure (MICP) measurements. The split used for XRD, TOC and MICP was further divided perpendicular to bedding so that each portion represents the same stratigraphic interval. For XRD and TOC analysis, the rock was crushed and a representative sample was prepared, whereas for MICP the rock was fragmented into larger particles (>5 mm) and measurements were performed on two sub-samples to check self-consistency. Details of preparation and selection of representative samples for SANS and USANS measurements is discussed in section A1 of the Appendix.

3.2 SANS and USANS instrumentations

SANS measurements were performed using three instruments at the Australian Centre for Neutron Scattering**,** Australian Nuclear Science and Technology Organisation: (1) the 40 m SANS instrument Quokka **(**Wood et al., 2018**)**, configured to three sample-to detector distances (1.4 m, 8 m and 20 m; neutron wavelength λ = 5Å) and a further configuration using MgF_2 focussing lenses (λ = 8.1Å), together covering the Q-range from $6x10^{-4}$ to 0.5 $Å^{-1}$; (2) the time-of-flight SANS instrument Bilby (Sokolova et al., 2019), working in the Q-range from $6x10^{-3}$ $Å^{-1}$ to 0.3 $Å^{-1}$; and (3) the USANS instrument Kookaburra (Rehm et al., 2013), configured for neutron wavelength λ = 2.37 Å and covering the Q-range from $2x10^{-5}$ to $2x10^{-3}$ $Å^{-1}$. SANS was measured using Quokka for L-type samples and Bilby for T-type samples. Pore size diameters measured by the Quokka SANS (2r = 5/Q, Radlinski et al., 2000) extended approximately from 1 nm to 830 nm, and the range probed by Bilby extended approximately from 0.3 nm to 50 nm**.** Pore size diameters measured using USANS ranged from 250 nm to 25 µm. SANS and USANS instruments jointly covered the pore diameter range from 1 nm to 25 µm, i.e. greater than five orders of magnitude. During SANS measurements at elevated pressures, the high Q-limit, $Q_{max} \approx 0.45$ $Å^{-1}$, was imposed by the environmental cell acceptance angle, which limited the maximal probed pore diameter to 2r ≈ 1.1 nm.

3.3 Experimental configurations for SANS and USANS

Pores in shales are often squashed in the out-of-bedding direction and the corresponding SANS spectra are anisotropic and axially symmetric about the axis perpendicular to the bedding plane. Therefore, three different sample orientations are necessary to gather microstructural information in 3D, as SANS and USANS reflect only the volume-average of structural features embedded in the scattering plane, i.e. the plane perpendicular to the direction of incident beam (Hall and Mildner, 1983; Gu et al., 2015; Gu and Mildner, 2016; Gu and Mildner, 2018; Blach et al., 2020).

Figure 1 illustrates the experimental configurations used for measurements of SANS (performed in pinhole geometry) and USANS (performed in double-crystal Bonse-Hart geometry). In this work the uniaxial stress measurements were performed using L-type samples (cut in-bedding-plane) in configuration called X (Fig. 1C). In configuration X, the sample may be rotated by any angle about the axis perpendicular to bedding and the scattering pattern will not be affected.

Images in the left column of Figure 1 illustrate sample orientation with respect to the bedding plane and the neutron beam direction (represented by the light blue arrow parallel to the z axis). A T-type sample shown in configuration Y (Fig. 1A) is rotated by 90° compared to configuration Z (Fig. 1B). Pictures in the right column show corresponding iso-intensity contours measured using a 2D SANS detector positioned perpendicular to the incident beam. The Q_x (and Q_y) range shown extends from 0 to about 0.1 Å^{-1}. The blue dot in the center represents the SANS instrument beam stop, which covers the Q-range from 0 to about 10^{-3}Å^{-1}. The yellow bar represents the slit-smeared Q-region contributing to USANS intensity measured at a fixed Q_x position of the detector. The width of the yellow bar is not drawn to scale; the effective USANS Q-range varies from ~10^{-5} Å^{-1} to ~10^{-3} Å^{-1}, with the HWHM (half width half maximum) resolution (ΔQ_x) of about 10^{-5} Å^{-1} and the slit-smeared ΔQ_y range of about ± 0.1 Å^{-1}.

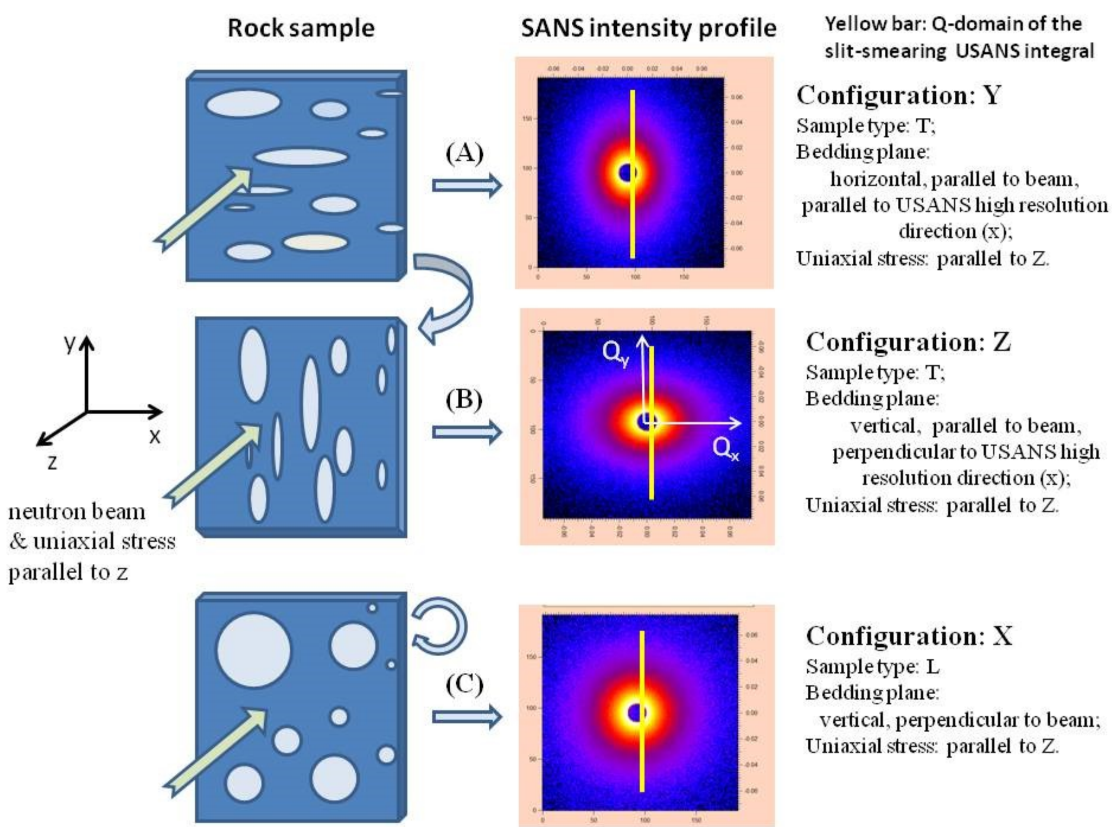

Figure 1. Schematic diagram of experimental configurations Y, Z and X used to measure 2D SANS and 1D slit-smeared USANS signal for anisotropic samples with axial symmetry.

For samples cut perpendicular to bedding (type T), USANS measurements were performed using configurations Y and Z, whereas 2D SANS data were acquired in configuration Y only. SANS and USANS data for samples cut parallel to bedding (type L) were acquired in configuration X. Configuration X enables measurements of L-type samples subjected to hydrostatic pressure (p) and/or uniaxial stress (S) in a geometry which simulates in-situ hydrostatic and lithostatic pressures. For T-type samples, configurations Y and Z may be used to simulate the effect of horizontal tectonic stress. Measurements of USANS in both the Y and Z configurations are needed to gain insight into the anisotropy of micrometer-size pores (Gu and Mildner, 2016).

Contrast matching measurements were performed at 23ºC in a deuterated methane atmosphere (CD_4 of purity 99.95, supplied by Cambridge Isotope Laboratories, MA, USA), using a stainless steel cell equipped with titanium windows, with no free volume in the path of neutron beam around the sample. For each sample, the cell was kept under dynamic vacuum for 1 hour prior to commencement of the first SANS or USANS measurement (performed at p=0 bar).

3.4 Supporting measurements

Simultaneously with SANS and USANS measurements, other analyses that inform about reservoir properites of shales were performed on the splits of the samples and they include X-ray diffraction (XRD), total organic carbon (TOC), porosity and permeability. These analyses were conducted not only to provide general characterization of the shale studied but also to scrutinize SANS data by comparison the results in the nanopore region.

Measurements of mercury porosimetry, porosity and permeability. For MICP analysis, samples were run using a Micromeritics AutoPore V 9620 mercury injection instrument at the Indiana Geological and Water Survey. The weight of dry samples ranged from 3–5 grams and the particle size was >5 mm to avoid porosity changes caused by crushing. Before analysis, the samples were dried at 85ºC for 24 hours. Two splits were analyzed and very good reproducibility of injection and withdrawal curves between the two splits was achieved. The pressure in the MICP instrument can reach 4137 bar (60,000 psi), probing pore throat sizes that range between 3 nm (0.003 μm) up to 9×10^5 nm (900 μm). After analysis, MICP data were corrected for conformance (mercury introduced around the sample at low pressures). To correct for this effect, all the mercury intruded at pressures below the capillary entry pressure (Po) was subtracted from the volumetric data (Sigal, 2009). Permeability in this study was determined using the Katz-Thompson method (Katz and Thompson, 1986). More details about this technique and experimental conditions are given in Mastalerz et al. (2021).

Porosity and permeability of the sample was also determined commercially by CORE LAB in Houston, USA. Bulk density of the core material was determined by mercury immersion. The sample was subsequently crushed and sieved through 20 and 35 US mesh sieves, and fraction >35 mesh was used in analysis. Grain density of shale samples was determined by measuring the weight and grain volume using the Boyle's Law double-cell technique with helium as the expansion gas. Porosity was calculated based on bulk density and grain density. Matrix permeability was determined by monitoring pressure decay which was recorded in 0.25 sec increments to a maximum time of 2000 sec. Matrix permeability of shale samples was determined using the Gas Research Institute method by monitoring pressure decay on clean and dry samples with a 20 to 35 mesh size range (Luffel et al., 1993). We note that determination of permeability of shales is a difficult task, and various techniques often provide very different results (Ghanizadeh et al., 2015a). Even though this method does not take into account the effect of confining pressure on the measured permeability values, it is one of the most commonly used on low permeability rocks.

XRD and TOC measurements. X-ray diffraction patterns of the whole rock and the clay fraction (< 4 μm) were acquired using a Siemens D5000 X-ray diffractometer with a SDD detector and a Scintag Pad-X X-ray diffractometer with a solid-state detector, respectively. Both diffractometers use Cu Kα radiation (40 kV, 40 mA). Powdered whole rock samples were scanned for 2θ from 2º to 60º at a scan rate of 1 degree/minute. The glycol-solvated clay-fraction mounts were analyzed over an angular 2θ range of 2 − 50 degrees at a scan rate of 1.5 degrees/minute. Semi-quantitative determination of the whole-rock and phyllosilicate mineral amounts was done by integrating the peak areas and utilizing the empirical reference intensity ratio factors, which were determined specifically for the diffractometers used for data collection.

A LECO elemental analyzer (SC832DR) was used to measure TOC contents of the samples. Approximately 1.00 g of powdered samples were weighed and treated with 10 wt. % HCl to remove carbonate minerals, and then rinsed with distilled water. The solid residues were freeze dried before TOC analysis. TOC contents of the residues were measured using a LECO elemental analyzer and then recalibrated to obtain TOC contents of corresponding original shale samples. Two analyses were run on each sample, and the average values were used for interpretation.

Low pressure gas adsorption measurements. Low-pressure gas adsorption measurements were conducted using a Micromeritics ASAP-2020 porosimeter and surface area analyzer. In both the N_2 and CO_2 adsorption techniques, the sample evacuation (degassing) time prior to analysis was 960 minutes and the target temperature was set for 110°C. For quantifying N_2 adsorption, the samples were analyzed at the liquid nitrogen temperature (77.35 K at 101.3 kPa). The adsorption branch was used to determine surface area, mesopore volumes and sizes. Among the parameters calculated from the N_2 adsorption analysis, BET surface area, Barrett-Joyner-Halenda (BJH) specific mesopore volume and mesopore size are discussed in this study. Following the published gas adsorption procedures (e.g., Usoltseva et al., 2014), the cross-section of the nitrogen molecule was assumed to be 0.162 nm^2.

For CO_2 adsorption, the temperature of the sample was set to 273.1 K by using a bath filled with a glycol and water mixture. The specific micropore volume, micropore surface area and micropore size distribution were determined based on the amount of adsorbed CO_2 at various pressure steps. In particular, Dubinin-Astakhov (D-A) specific micropore volumes and micropore sizes were recorded. The relative (P/P_0) pressure ranged from 0 to 0.03, which corresponds to the absolute pressure of ~2 to 784 mm Hg (0.266 to 104.5 kPa). More detailed dscription of the low-pressure gas adsorption methodology is provided elsewhere (Mastalerz et al., 2017).

4. Results and Discussion

4.1 Anisotropy of pores

The PDSP model-based analysis of SANS/USANS results for Marcellus shale assumes isotropic (spherical) pores. This is an approximation, since pores in shales are statistically isotropic along bedding planes, and on average are distorted in the direction perpendicular to bedding. Therefore, the pore size distribution, porosity, specific surface area and the pore volume distribution computed in this work from SANS/USANS results acquired in configuration X illustrated in Figure 1C are only apparent, as they have been obtained assuming pore geometry in the out-of-bedding direction to be the same as in-bedding. To quantify the pore deformation, additional SANS and USANS measurements were performed in configurationY (Fig. 1A) and Z (Fig. 1B)) on samples cut in the direction perpendicular to bedding: T3 of thickness 1.03 mm and T5 of thickness 0.83 mm. Figure 2(A) shows the scattering intensity with a large-Q background of 0.18 cm^{-1} subtracted. Additional details, including power-law fits, are shown in Fig 2(B) for the SANS Q-range from $2x10^{-3}$ to 0.2 $Å^{-1}$ and in Fig. 2(C) in the USANS Q-range from $8·10^{-5}$ to $2·10^{-3}$ $Å^{-1}$. Since the (desmeared) USANS results (Figure 2C) as well as sector-averaged SANS results (Figure 2B) in the Q_x and Q_y direction for configurations Y and Z do not coincide, it follows that pore orientation is preferred and they are are indeed flattened in the out-of-bedding direction. USANS results, obtained in a separate study for Marcellus_7084 samples of various thickness indicate that for samples T3 and T5 there is no discernible distortion caused by multiple scattering for $Q > 3 \cdot 10^{-5}$ Å^{-1}.

The relationship between the pore anisotropy and the shape of the three-dimensional small-angle scattering iso-intensity surfaces has been discussed in several papers, most recently by Gu and Mildner (2016), Gu and Mildner (2018), Blach et al. (2020) and Cherfallot et al. (2020). For rocks exhibiting power-law SANS scattering over an extended Q-range along the main axis of the scattering ellipsoid (as in Fig. 2), the most suitable anisotropy measure is the intensity ratio, $\mathscr{R}(Q) = I(Q; Z) / I(Q; Y)$ (Blach et al. 2020). For such systems, for each Q-value, $\mathscr{R}$ is approximately equal to the ratio of two projections of the rock-pore interface area, S: $\mathscr{R} = S_T/S_L$, where subscripts T and L indicate planes perpendicular to the bedding and parallel to bedding, respectively. For instance, a spherical pore of radius b squashed in the out-of-bedding direction becomes an oblate spheroid, and the third semi-axis, c, becomes smaller than b. Therefore, the pore surface projection on plane L is $\pi \cdot b^2$, and the projection on plane T it is $\pi \cdot c \cdot b$ (for the sake of argument assuming that pore dimensions in the L-plane are confined). For this case $\mathscr{R} = S_T/S_L = c/b$, and, importantly, $\mathscr{R} = V_{os} / V_{sph}$, where V is the pore volume (where the subscript 'os' denotes oblate spheroid and subscript 'sph' indicates a sphere of radius b). Consequently, the value of $\mathscr{R}$ can be also considered an approximate correction factor for the pore volume distribution obtained from SANS/USANS measurements performed on samples cut in-bedding in configuration X.

(A)

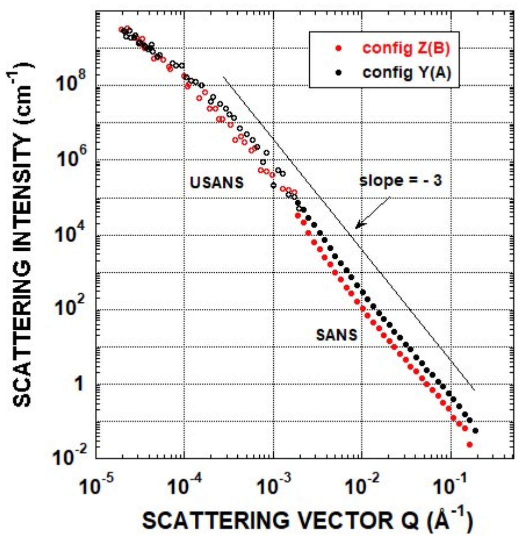

(B) (C)

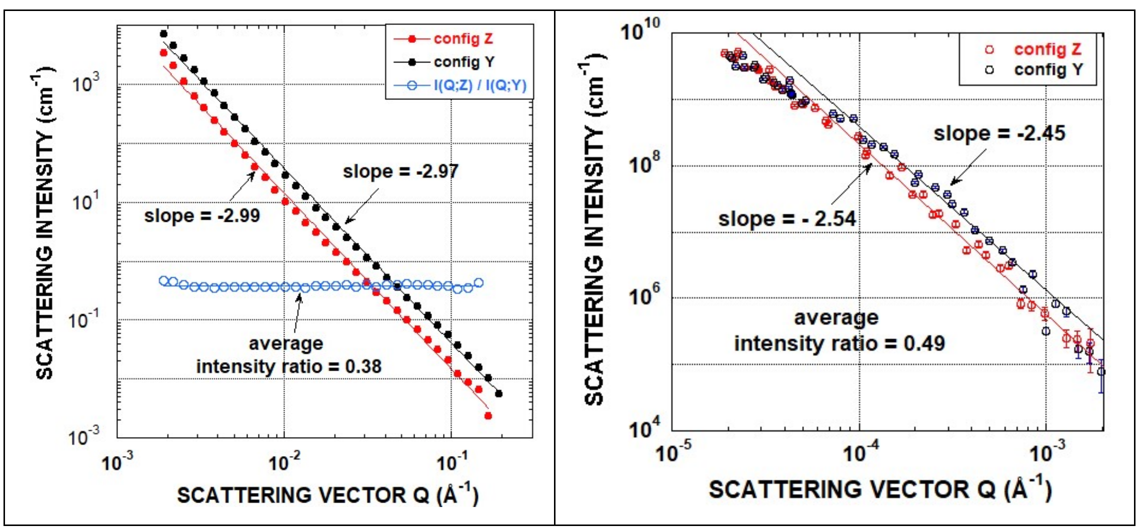

Figure 2. Graphs of (±15º sector-average) SANS and (desmeared) USANS scattering for Marcellus_7084 samples T3 and T5 measured in configurations Y and Z in ambient conditions. (A) - combined SANS and USANS data with the large-Q background of 0.18 cm^{-1} subtracted; (B) SANS intensity for configurations Y (black dots, fitted power-law slope = 2.97) and Z (red dots, fitted power-law slope = 2.99), and the Y-to-Z scattering intensity ratio (blue circles, average value = 0.38); (C) USANS scattering intensity for configurations Y (black circles, fitted power-law slope = 2.45) and Z (red circles, fitted power-law slope = 2.54); the power-law fit was done for Q > 8x10^{-5} Å^{-1}; the average Y-to-Z intensity ratio is 0.49. In all panels, the statistical error for SANS intensity is much smaller than the symbol size; for USANS, the error is comparable to symbol size for Q ≤ 1x10^{-3} Å^{-1}.

For sample Marcellus_7084, the intensity ratio is $\mathscr{R}$ = 0.38 for pore diameters from ~2.5 nm to ~250 nm (mesopores) and $\mathscr{R}$ = 0.49 for pore diameters from ~500 nm to ~6 µm (macropores). The transition occurs for pore sizes similar to the average grain size and is most likely related to different pore space geometry for the inter-grain and intra-grain pores.

The degree of pore anisotropy in Marcellus shale samples has been quantified by various authors (e.g., Guo et al., 2015; Guo and Mildner, 2018) . The most often used measure is the eccentricity of the SANS intensity profile, ε, defined as the ratio of the short axis to the long axis of the isointensity SANS ellipsoid (Fig. 1, configurations Y and Z). Since $\varepsilon = \mathscr{R}^{1/n}$, where n is the power law exponent on the I(Q) versus Q plot (Blach et al. 2020) and the average value of n is 2.98 for mesopores (Fig. 2B) and 2.5 for macropores (Fig. 2C), it follows that ε is 0.72 for mesopores and 0.75 for macropores. For comparison with other ε-values determined for Marcellus shale, Gu et al. (2015) reported ε = 0.63 and Gu and Mildner (2018) ε = 0.66 to 0.68. In those studies, however, a significant variation of anisotropy with ore size was observed; this is not the case for sample Marcellus_7084 measured in this work. These observations suggest that for the Marcellus shale, the degree of pore anisotropy can vary depending on location. It is important to evaluate it for each site since it does influence the pore accessibility, gas diffusion and the fluid transport behavior during gas production (Zhang et al., 2020).

4.2. Accessible and inaccessible porosity

4.2.1 SANS / USANS data at ambient and contrast matching conditions

Figure 3A illustrates joined SANS and USANS curves (obtained in configuration X for L-type sub-samples L6 and L4, respectively), measured in vacuum and at the full contrast matching pressure of 500 bar of CD_4. The shapes of the curves indicate an approximate power law scattering, with the power exponent varying from about -3.4 in the Q-range from 0.05 Å^{-1} to $5 \cdot 10^{-4}$ Å^{-1} (corresponding to pore diameters, 2r = 5/Q, from ~10 nm to ~1000 nm) to about -2.1 for 2r ≥ ~1000 nm. Such a change is typical for fine-grained sedimentary rocks; it reflects a transition from surface ($D_s \approx 2.6$) to mass fractal geometry ($D_m \approx 2.1$ in this case) as the scale of observation, of the order of 1/Q, exceeds the volume-average grain size (about 1 µm in this case).

The intensity of neutron scattering at ambient conditions is a sum of scattering from the accessible and inaccessible pores, whereas the intensity measured at the full contrast match condtions corresponds to scattering from the inaccesible pores only. For pore diameters 10 nm < 2r < 1000 nm the two curves nearly coincide (Fig. 3A), therefore the relative number of accessible pores must be small. In the macropore region, the fraction of accessible pores gradually increases as the pore diameter increases from 1 µm to ~25 µm.

In the large-Q region, the I(Q; ambient) curve flattens out into the so-called "flat background" (Fig. 3B). Details are discussed in Section A2 of the Appendix. In the following we demonstrate that choice of the "flat background" strongly affects values of microstructural parameters.

(A) (B)

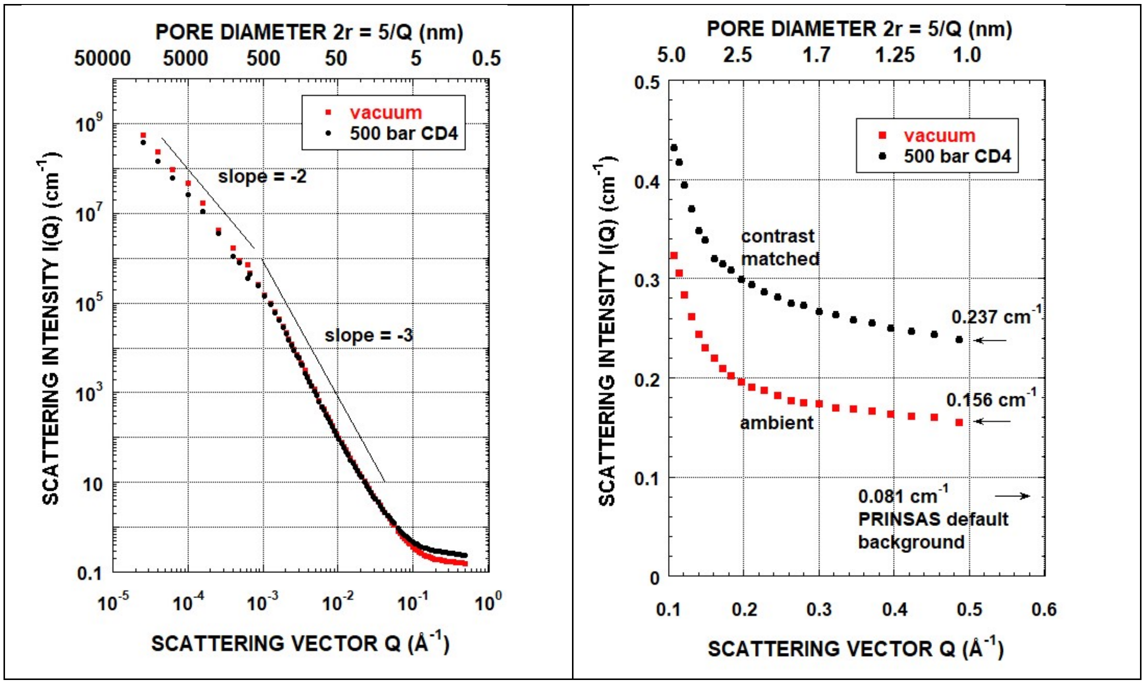

Figure 3. (A): Graphs of combined SANS and USANS absolute scattering cross section (scattering intensity) measured for samples Marcellus_7084 L6 (SANS) and L4 (USANS) in vacuum (red circles) and at 500 bar of CD_4 (contrast matched, black points). (B): Large-Q detail of the SANS data. Arrows indicate a position of the large-Q flat background subtracted before fits to a nano-structural model (here: 0.156 cm^{-1} for p = 0 and 0.237 cm^{-1} for p = 500 bar) and the PRINSAS default background obtained using the "find background" automatic option (here 0.081 cm^{-1}). For detailed discussion see text. Statistical error for USANS is similar to the symbol size, and much smaller than symbol size for SANS (see Fig. 2).

4.2.2. Accessibility of pores to methane calculated from neutron scattering data

The fraction of pores accessible to penetrating fluid, $F_a(r) = N_a(r)/N(r)$, can be quantified from SANS/USANS data acquired at the ambient and full contrast match conditions using Equation A1 (section A2 of the Appendix). Equation A1 holds true as long as the fluid density in pores accessible to methane is equal to the density of penetrating gas and, consequently, $I(Q;\{CM\}) \leq I(Q;\{ambient\})$. For sample Marcellus_7084, this takes place for mesopore diameters larger than about 25 nm (in the "bulk density of CD_4" region of Figure 4). Results obtained from Eq. A1 indicate that in this region $F_a = 0.06 \pm 0.02\%$. It follows that only a fraction of 0.06 of mesopores with diameter in the range from 25 nm to 500 nm are accessible to methane. For the macropores, however, F_a gradually increases up to 0.35 as the diameter increases. It appears that in the pore diameter range 25 nm $\leq D \leq$ 20 µm the values of $F_a(2r)$ are consistent with the density of CD_4 confined in pores being equal to the bulk density of gas at the full contrast match pressure of 500 bar.

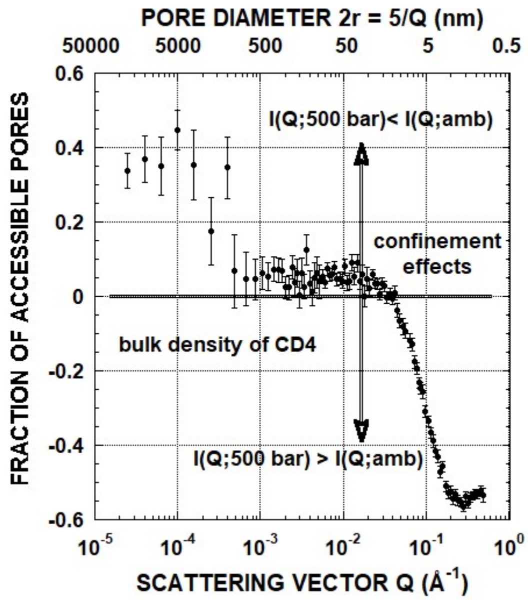

Figure 4. Plot of the apparent fraction of accessible pores, F_a, calculated for the sample Marcellus_7084 according to Eq. A1. The region of pore sizes containing gas with the bulk pressure and density values is delineated from the nanopores which host gas of higher density (increasing as the pore size decreases due to the influence of confinement effects) by the vertical double arrow. The borderline is located at $Q \approx 2\text{x}10^{-2}$ Å^{-1}, which corresponds to the nanopore diameter of ~25 nm. Pore diameters, calculated for every full decade of Q-values, are displayed above the top horizontal axis. Negative values of F_a are an artefact discussed in the text.

However, for nanopores smaller than ~25 nm ($Q > 0.02$ Å^{-1}) the experimentally determined nominal value of $F_a(r)$ (= 1 - [I(Q;{CM}) / I(Q;(amb)], where r = 2.5/Q) becomes negative, which is attributed to the increased gas density in confinement; this condensation effect violates the full CM condition for nanopores smaller than ~25 nm. Regardless of the mechanism (discussed in section A3 of the Appendix), the increasingly negative value of $F_a(r)$ as r decreases demonstrates that methane penetrates the accessible SDN (Single Digit Nanopores) down to a diameter of at least 1 nm, and the pore-volume-average density of confined CD_4 gradually increases as the pore size decreases. This observation directly confirms the existence of accessible nanopores, including SDN, and accentuates their importance as the gas storage sites.

Formalism of estimation of the density of methane in confinement is described in section A3 of the Appendix. The model of CM SANS intensity based on a uniform pore filling mechanism predicts that methane (externally supplied at the full CM pressure of 500 bar) densifies by a factor from 2.3 (for Fa =1) to 4.2 (for Fa = 0.06) when confined in the nanopores, which results in the density of confined CD_4 from 0.78 to 1.43 g/cm^3, respectively. The lower value is significantly larger than d(CD_4) ≈ 0.60±06 g/cm^3 estimated by Eberle et al. (2016) for 1-2 nm SDN at p=345 bar. In addition, for Marcellus_7084, the model predicts confined density at the upper end of the range, given the low starting value of F_a measured at the 25 nm borderline. The nominal gas pressures corresponding to the prediced density range are from 5.5 kbar to the highly unlikely value of 200 kbar (Ramsey, 1963). It is concluded that the uniform pore filling mechanism does not explain the large intensity of the SANS signal measured at contrast match (500 bar of CD_4) for nanopore diameters from 1 nm to ~15 nm. A similar conclusion was reached for methane condensation in highly accessible nanopores of the Barnett shale by Ruppert et al. (2013), who proposed that condensation leads to formation of separate nano-size clusters rather than a continuous phase uniformly filling the pore space. This is akin to a nucleation and growth mechanism, most probably starting on hydrocarbon-wet surface sites. In addition, recently Neil et al. (2021) observed a methane-pressure-induced formation of CD_4 nano-size clusters in overmature Marcellus samples and interpreted their results of pressure-cycling CM SANS measurements as a consequence of the molecular methane becoming trapped in the kerogen stucture.

4.2.3. Formation of high-density gas nano-clusters at elevated pressure of methane

As mentioned above, it is proposed that pressure-induced formation of additional (excess) large-density methane nano-clusters takes place Marcellus_7084. Figure 5A shows the full SANS/USANS curve, measured at the ambient and full CM conditions in configuration X on a L-type sub-sample (with the large-Q backgrounds subtracted). The large-Q (nanopore) region of the SANS data is shown in Fig. 5B. The difference, I(CM) - I(amb), magnified by a factor of 100, is also shown there. In this nano-scale region, extending

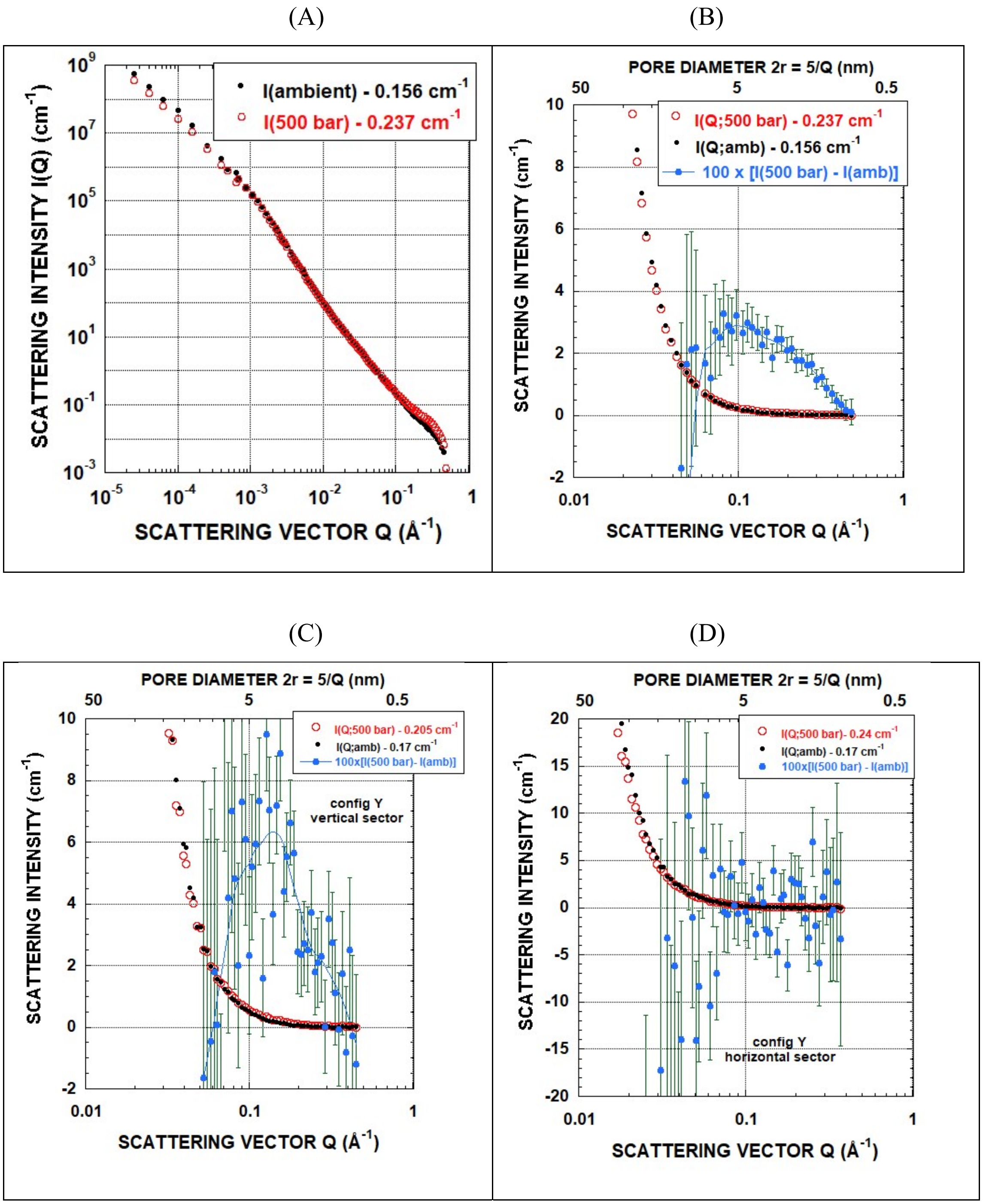

Figure 5. SANS and USANS results acquired at ambient conditions and contrast matched (p = 500 bar of CD_4) for L-type (parallel to bedding) and T-type (perpendicular to bedding) slices of Marcellus_7084. The large-Q background is subtracted. (A) - combined desmeared USANS and radially-averaged SANS data (L-type sample, configuration X); statistical error is smaller than symbol size. (B) - the large-Q region of (A) and I(500 bar)-I(amb), multiplied by a factor of 100 (blue dots). (C) - sector-averaged [I(500 bar)-I(amb)]x100 data (T-type sample, configuration Y, vertical sector ±15º). (D) - sector-averaged [I(500 bar)-I(amb)]x100 data (T-type sample, configuration Y, horizontal sector ±15º). Blue lines were generated using the automatic option of "smooth fit" to data points and serve as guide for the eye only. For definition of configurations refer to Fig.1.

from ~1 nm to ~40 nm and dominated by confinement effects, at CM conditions there is an excess asymmetric broad peak, extending from Q = 0.06 Å^{-1} to 0.4 Å^{-1} (with half-width half-maximum, HWHM, equal to about 0.19 Å^{-1} on the large-Q side) and centered at Q_{max} = 0.09 (±0.1) Å^{-1}. This peak is evidence for pressure-induced formation of an additional population of methane-filled pores (or clusters), with diameters distributed from 1 nm to 8 nm (measured in-bedding-plane), and the maximum number density at the diameter $5/Q_{max}$ of about 5.5 (±0.5) nm. This relatively weak peak (height ~0.03 cm^{-1}) is superimposed on a much stronger large-Q SANS background (0.237 cm^{-1}). A fraction of 0.081 cm^{-1} (equal to 0.237 cm^{-1} minus 0.156 cm^{-1}) of that background originates from scattering on pre-exiting accessible nanopores which, at ambient conditions contributed to the large-Q background of 0.156 cm^{-1} and, at contrast match, became filled with CD_4.

A similar excess asymmetric peak (Fig. 5C) is observed in configuration Y for sector average of SANS data in the Q_y direction (Fig. 1). This experimental orientation reveals the size distribution of pressure-induced clusters measured in the direction perpendicular to bedding. Statistical scatter of experimental data is now greater than in Fig. 5B as only a fraction of experimental counts recorded by the 2D detector were used for sector averaging. The position of the peak appears to have moved to about 0.14 (±0.02) Å^{-1} (2r ≈ 3.6 (±0.5) nm); its HWHM on the large-Q side is about 0.08 (±0.02) Å^{-1} and its magnitude is about 0.06 cm^{-1}. The peak is superimposed on the background that increased by 0.035 cm^{-1} between the normal and contrast matched conditions (from 0.17 cm^{-1} to 0.205 cm^{-1}).

This indicates that within uncertainty, size distribution of the excess clusters are wider in the bedding plane direction than in the direction perpendicular to bedding. Using a simple analogy, the shape of the excess clusters can be imagined as nano-size discs embedded in the rock matrix, which are statistically oriented parallel to bedding, have a wide diameter distribution (with a broad maximum at 2r ≈ 5.5 (±0.5) nm) and a more narrowly distributed thickness centered at ~3.6 (±0.5) nm.

Importantly, comparison of the size of the excess peak in configurations X (0.03±0.01 cm^{-1}) and the vertical section of Y (0.07±0.01 cm^{-1}) with the increase of the background scattering (0.081 cm^{-1} and 0.035 cm^{-1}, respectively) indicates that, at the contrast matched pressure of 500 bar, a significant fraction of confined methane has condensed into the SDN clusters at sites that were not detected at ambient conditions. Detailed quantitative analysis would require assumptions in regard to the nanopore geometry and the density of confined CD_4 in the SDN region (Bahadur et al., 2015; Eberle et al., 2016) .

Figure 5D shows the large-Q (nanopore) region of SANS data for the same sample as in Fig. 5C, but sector-averaged in the Q_x direction (parallel to bedding). SANS theory predicts that data shown in Figs. 5D and 5B should be identical (Radlinski et al. 2004b; Gu and Mildner 2018); however, the scatter of data in Fig. 5D is too extensive for a meaningful conclusion. Nonetheless, we note that the large-Q background at contrast match for the Q_x sector average (0.24 cm^{-1}; Fig. 5D) is similar to the configuration X azimuthal average background of 0.237 cm^{-1} (Fig. 5B) but significantly greater than the background measured for the Q_y sector average (0.205 cm^{-1}; Fig. 5C).

Provided that the pore-volume-average SLD of gas ($\rho_g(r)$), confined in uncorrelated pores of different sizes is known, the excess number of nano-clusters could be quantified using modified Eq. A3:

$$I(Q; CM) - I(Q; ambient) = \int_0^\infty N_{exc}(r)\,[v(r)]^2\,F_0(Q,r)\,\left(\rho_g^2 - 2\rho_m\rho_g\right)dr \quad (7)$$

where $N_{exc}(r)$ is the number density of the contrast-match-activated excess nano-clusters. In this work we do not attempt the fit given lack of reliable data pertaining to the pore shape and gas density in the SDN region. However, the cross-over of the I(Q; ambient) and I(Q; CM) curves in the large-Q region is a common phenomenon, which has been previously reported for CM SANS results using CD_4 for various rocks, e.g. coal (Melnichenko et al., 2012; He et al, 2012); shale kerogen (Chiang et al., 2018) and Marcellus Shale (Eberle et al., 2016; Neil et al., 2020; and Jubb et al., 2020, for the 2307 m sample). It is possible that detailed analysis of the large-Q SANS data would reveal a similar mechanism of clustered methane condensation.

Our results suggest that at the elevated pressure of methane (and at contrast matched conditions in particular) isolated nano-clusters of condensed methane are forming in addition to gas condensation in the nanopores which are accessible at ambient conditions. The physical location of nano-clusters has not been determined; it could be in the accessible nanopores (hosted in the organic and/or mineral matter), but could also include isolated sites with high affinity for hydrocarbons located anywhere in the pore space, and/or semi-closed SDN (single digit nanopores) in organic matter that become partly occupied only at elevated pressure. The latter sorption mechanism would be sensitive to the pressure-controlled geometry of the organic matter (bitumen), as suggested by Neil et al. (2021).

4.2.4. Total accessible and inaccessible porosity: the large-Q background problem

Total porosity, ϕ, was determined using two methods - as a sum of volumes of all pores calculated using the PDSP model (PRINSAS software, Hinde 2004) and directly from the Porod Invariant, PI:.

$$PI = \int_0^\infty Q^2 I(Q)dQ = 2\pi^2 (\Delta\rho)^2 \phi(1-\phi) \quad (8)$$

Apparent porosities were calculated from the combined SANS and USANS results acquired in configuration X for L-type samples at ambient conditions (for all pores, accessible and inaccessible) and at contrast matched conditions (for inaccessible pores only). Calculations were performed assuming the experimentally determined matrix SLD value of 3.4×10^{10} cm^{-2} for Marcellus_7084, which matches the SLD value independently determined for isolated Marcellus kerogen (Thomas et al. 2014), thus justyfying the use of the two-phase approximation (Eq. 1 and Eq. 8). Owing to uncertainty of the magnitude of the large-Q background that should be subtracted from experimental data before fitting to structural models (section A2 in the Appendix), calculations were performed for a range of possible background values, from 0 to $I(Q_{max})$ (0.156 cm^{-1} at ambient conditions and 0.237 cm^{-1} at contrast matched conditions). Porosity was determined using I(Q) data acquired in the full

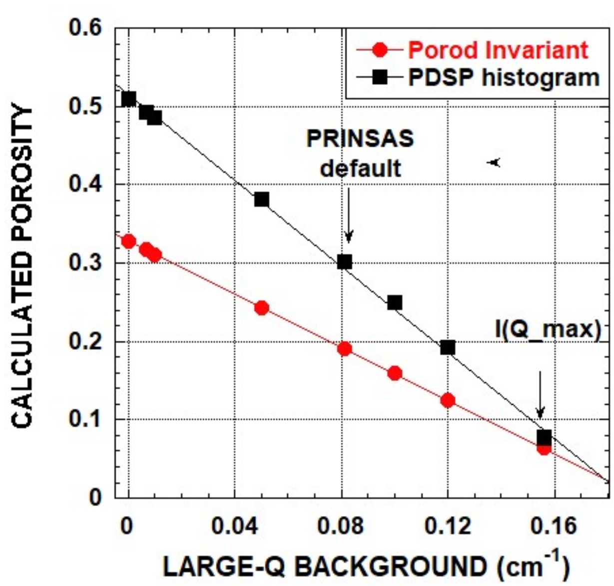

Figure 6. Apparent total porosity versus large_Q background calculated for sample Marcellus_7084 from joined SANS-USANS absolutely calibrated data. Calculations were performed in the Q-range from 2.5×10^{-5} Å^{-1} to 0.5 Å^{-1} using two methods: the PDSP model (full black squares) and model-free Porod Invariant (open red squares).

experimental Q-range ($2.5x10^{-5}$ $Å^{-1}$ to 0.5 $Å^{-1}$), which corresponds to the pore size (diameter) range from 1 nm to 20 μm, where the diameter 2r is equal to 5/Q. The results demonstrate that the choice of a particular value for the large-Q background may have a dramatic effect on calculated porosity (Figure 6).

The PDSP and PI curves do not coincide in Figure 6, which we attribute to a systematic error caused by the deteriorating numerical accuracy of the PRINSAS fit at the large-Q limit for decreasing background values. In contrast, porosity based on PI (Eq. 8) is always computed with the same accuracy. As expected, the two values coincide at the upper limit of the background, $I(Q_{max})$ (Fig. 3B). $I(Q_{max})$ is often selected as the 'true' background, although it is a somewhat arbitrary choice forced by the limited acceptance angle of the SANS experimental system (instrument or environmental cell). Another frequently used background value is B, the default 'fractal' background automatically calculated using the 'find background' PRINSAS option, which is obtained from a fit to Equation 2. It should be only used when only the fractal subset of the pore space is of interest (therefore the Q-range is limited such that I(Q) follows the power law with good accuracy and the large-Q flat background is not reached, hence cannot be directly determined). Finally, the lowest theoretically possible background value is due to incoherent scattering, estimated for ~0.0068 cm^{-1} for the Marcellus_7084 core.

Considering the PI-determined trend in Figure 6 to be more accurate than the PRINSAS estimates, the SANS/USANS-based total porosity value for Marcellus_7084 (accessible plus inaccessible) is contained within the limits from 5.9% to 31.7%. The actual 'true' value depends on the contribution from physically existing pores as opposed to the non-porous small scale inhomogeneities, described in section A1. The range can be narrowed using values obtained for accessible porosities with invasive methods that employ probes of different sizes and chemical affinities, e.g. MICP and helium porosimetry (Table 2).

To summarize, the total SANS/USANS ambient porosity is included in the range from 6% to 31%, and about 6±2% of all pores are accessible to methane (Fig. 4). Note that the apparent inaccessible porosity calculated from the contrast matched data listed in Table 2 is larger than the total porosity calculated from ambient data, which is an artefact caused by the excess scattering in the ~5 nm pore size region (Fig. 5B); hence the negative values for the apparent accessible porosity in the first two rows of Table 2. The accessible-to-mercury MICP porosity is 1.68%, and the porosity accessible to helium is 6.88%. These numbers cannot be directly compared with the SANS/USANS porosity owing to different pore size ranges (Table 3).

Table 2. Range of calculated apparent accessible and inaccessible SANS/USANS porosity for sample Marcellus_7084 (sub-samples L4 and L6), and the accessible porosity results obtained using MICP and helium porosimetry. B_S is the large-Q background (in cm^{-1}) subtracted from experimental SANS/USANS data prior to porosity calculations.

Method of calculation	**Pore size range (nm)**	**Ambient: total porosity $\phi = \phi_i + \phi_a$ (%)**	**Contrast matched: inaccessible porosity ϕ_i (%)**	**Accessible porosity ϕ_a (%)**
Porod Invariant	2.0 – 20,000 (pore body)	5.1 ± 0.5 B_S = 0.156	5.2 ± 0.5 B_S = 0.237	-0.1±0.7
Porod Invariant	1.0 – 20,000	6.4 ± 0.5 B_S = 0.156	7.5 ± 0.5 B_S = 0.237	-1.1 ± 0.7
Porod Invariant (range)	6.0 – 20,000	6.4 to 31.7 B_S = 0.0068 to 0.156	7.2 to 34 B_S = 0.081 to 0.237	0 to 28
MICP	3.0 – 20,000 (pore throat)			1.68
Helium porosimetry	D > 0.26 (pore body)			6.88

It seems reasonable to assume that the porosity accessible to methane, ϕ_a, is close to the lower end of the MICP-helium range of 1.68% < ϕ_a < 6.88%, but it leads to a rather unrealistic total porosity (accessible plus inaccessible) of the order of 20%. However, mercury porosimetry is an invasive method that can cause deformation of the inorganic matrix and kerogen structure at high pressures (Li et al. 1999), including the critical nanopore structure. Likewise, helium porosimetry measurements reported here were performed on crushed material and it is possible that mechanical treatment helped to open gas access to some of the nanopores not accessible in the solid core (Mastalerz et al. 2017). The accessible porosity provided by He porosimetry is an overestimate for methane for two additional reasons: (1) the kinetic diameter of the CH_4 molecule (0.38 nm, possibly larger for deuterated methane CD_4) is much larger than for the helium atom (0.28 nm; Baker 2012) and (2) the surface affinity for methane is higher for kerogen than the clay mineral sites (Fan et al, 2014). This indicates the importance of nanopore characterisation in shale using non-invasive methods; their further development requires addressing the yet unresolved issue of separating various contributions to SANS intensity in the nanopore region, especially to the large-Q background. In the following we provide fits of the ambient and contrast matched data to the PDSP model (using

PRINSAS software), where, for want of a better option, we follow the usual practice of taking $I(Q_{max})$ as the large-Q background value.

4.3. Microstructural parameters from fits to the PDSP model

Pore size distribution. The probability density function for pore radii, f(r), was calculated for the accessible and inaccessible pores following the PDSP model (coded in the PRINSAS software; Hinde 2003). Results are shown in Fig. 7. Distributions calculated for CM and ambient conditions are practically identical, and over the entire pore size range can be approximated by a power law function with a slope of -4.14. This is roughly consistent with the slope of about -4.0 (equal to $-(1+D_s)$) predicted from Eq. (3a)), where $D_s \approx 3.0$ is obtained from the slope of the log(I(Q)) versus Q plot (equal to $D_s-6 \approx -3.0$ for $Q > 3 \times 10^{-4}$ Å^{-1}, hence $D_s \approx 3.0$; Fig. 2B and Fig. 3A). In addition, the close similarity of both distributions is consistent with the pore space being dominated by inaccessible pores.

Specific surface area for the accessible and inaccessible pores. In addition to the distribution of f(r), Fig. 7 shows the variation of the internal specific surface area with the probe size, calculated (and extrapolated to small probe diameters) for all pores (accessible plus inaccessible, calculated from ambient data) and for inaccessible pores (calculated from contrast matched data). In the pore radius range 2 to 10 nm (20 to 100 Å), the two curves practically coincide within a statistical error of ±10%, thus indicating that the surface area (SSA) associated with accessible porosity is no more than about 15% of the total SSA. The total SSA is estimated as 39 m^2/g for the probe diameter of 0.4 nm (close to kinetic diameters of gases as well as effective molecular diameters, Table 3). As expected, the SANS/USANS SSA value for accessible plus inaccessible pores is much greater than the accessible SSA (of 3.3 to 8.8 m^2/g) determined using MICP and nitrogen adsorption. The relatively large value of SSA determined using adsorption of CO_2 (19.3 m^2/g) confirms the general observation that a large fraction of accessible porosity is contained in single digit nanopores (with diameter < 2 nm). The larger SSA obtained with CO_2 adsorption results from better penetration into the multi-size pore structure as compared to N_2. Even though these two molecules are similar in size (gas kinetic diameter of N_2 and CO_2 are 0.364 nm and 0.33 nm, respectively; Baker 2012), the much higher temperature during CO_2 adsorption analysis is the main reason for easier access to the smallest pores and more effective adsorption (Gregg and Sing, 1982; Rouquerol et al., 2014; Mastalerz et al., 2017).

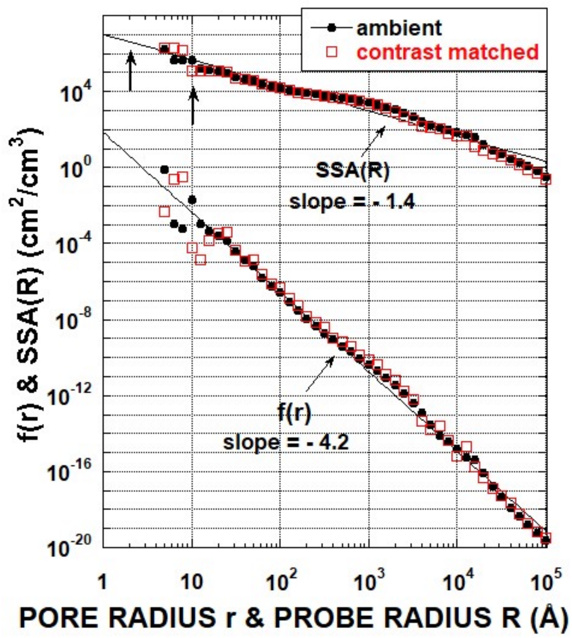

Figure 7. Probability density function of apparent pore radii, f(r), calculated using the PDSP model from combined SANS and USANS data acquired at ambient conditions (full black circles) and at contrast matched condition (open red squares), and the apparent specifc surface area, SSA(R), for various molecular probe sizes. Results were computed using the PDSP model from combined SANS and USANS data. Arrows indicate molecular probe radii 0.2 nm (2 Å) and 1 nm (10 Å).

Table 3. Values of the specific surface area for sample Marcellus_7084_L6 obtained using different methods. Two estimates of the gas probe sizes are shown: (^{a}) gas kinetic parameter (Baker, 2012) and (^{b}) effective molecular diameter for supercritical fluid at 20 ºC (Ben-Amotz and Herschbach, 1990).

Method	Probe size (nm)	SSA (m^2/g)	Pore type
SANS/USANS (extrapolated)	0.4	39	all
SANS/USANS (extrapolated)	2	6.8	all
MICP IU mercury	0.3058	3.25	accessible
ASAP 2020 nitrogen BET	0.364^a ; 0.345^b	5.39	accessible
Langmuir		8.73	
BJH		4.43	
ASAP 2020 CO_2 (micropore)	0.33^a; 0.348^b	19.3	accessible

Incremental pore volume and comparison with the MICP data. Fig. 8 shows the apparent incremental pore volume, dV/dr, for all pores and inaccessible pores, calculated using the PDSP approximation for matrix density of 2.55 g/cm^3. The quantity dV is the incremental volume of pores with radii inside the interval [r, r+dr]; $dV_x = N_x(r)\cdot v(r)$, where the subscript 'x' is substituted by 'tot', 'in' or 'ac' for all pores, inaccessible pores and accessible pores, respectively; $N_x(r)$ is the number density (concentration) of pores with radii in the interval [r, r+dr], and v(r) is volume of the pore of size r ($v = 4/3 \cdot \pi\ r^3$ for spherical pores used in the PDSP model). We note in passing that the fraction of accessible pores, $N_{ac}(r)/N_{tot}(r)$ is equivalent to the ratio of $(dV_a(r)/dr)/(dV_{tot}(r)/dr)$.

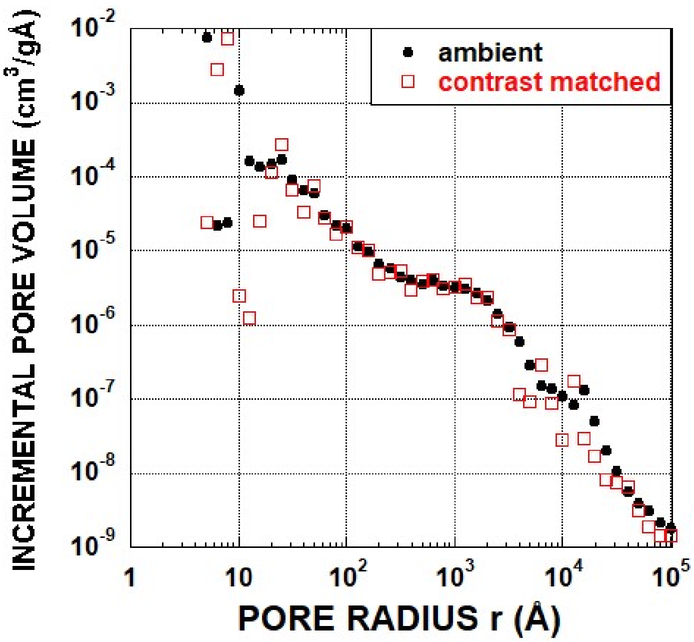

Figure 8. Incremental pore volume of all pores (ambient, full black circles) and inaccessible pores (p = 500 bar of CD_4 at contrast matched conditions, open red squares) calculated from combined SANS and USANS results according to the PDSP model.

The results presented in Figure 8 clearly indicate that the smallest nanopores (including the SDN) make the greatest contribution to total porosity. Results for the accessible plus inaccessible pores are calculated from the SANS/USANS data acquired at the ambient (total = accessible plus inaccessible) and contrast matched conditions (inaccessible) in the entire range of pore sizes, using the large-Q background values shown in Fig. 3A (the choice of the background for I(Q) does not affect the derivative dV/dr for pore radii > 3 nm (30 Å)). The two sets of data shown in Fig. 8 appear similar considering the scatter of calculated values of dV/dr, perhaps with the exception for pores with radii larger than ~500 nm ($5x10^3$ Å). This is consistent with previous observation that the difference between the ambient and contrast matched scattering intensity in the mesopore region is only about 6% (Fig.4), which indicates that great majority of pores are inaccessible to methane.

Direct comparison between the SANS and MICP dV/dr data is presented in Fig. 9A. Interpretation, however, requires caution since the SANS and MICP experimental results have been processed according to different pore shape models (polydisperse spheres for SANS, polydisperse cylinders for MICP), which only approximately reflect the statistically oblate spheroidal (squashed) shape of pores in Marcellus_7084 (section 3.1). Consequently, SANS results are plotted against the apparent pore body radius, r_b, whereas the MICP data against the pore throat radius, r_t. The ratio r_b/r_t may be pore-size dependent; it is not known for tight shales - one can only reasonably assume that $r_b/r_t \geq 1$ (it is about 3.5 for high porosity sandstones (Radlinski et al., 2004). To sum up, we compare (i) $(dV/dr)_{tot}$, calculated from SANS/USANS data acquired at ambient conditions, for all pores (accessible plus inaccessible, Fig. 8 and Fig. 9A), and (ii) $(dV/dr)_{in}$, determined from SANS/USANS acquired at the pressure p = 500 bar of deuterated methane, for methane-inaccessible pores (contrast matched conditions, Fig. 4 and Fig. 9B), and (iii) $(dV/dr)_{ac}$, determined from MICP data acquired at mercury pressures in the range 2 to 4130 bar (30 to 60,000 psia) for mercury-accessible pores (Fig. 9A and Fig. 9C). For clarity, the relevant results are re-plotted in Fig. 9(A-C).

Figure 9A shows a direct comparison of the dV/dr results calculated from MICP and SANS. Figure 9B (a modified Fig. 4) shows a plot of the fraction of accessible pores, $N_{ac}(r)/N_{tot}(r)$, determined from SANS, and Fig. 9C shows the same fraction, calculated as $(dV_a(r)/dr)/(dV_{tot}(r)/dr)$, using the SANS and MICP experimental results presented in Fig. 9A. Results presented in Figures 9A, 9B and 9C are clearly inconsistent: accessibility for methane at p = 500 bar dramatically decreases with the pore size (Fig.9B), whereas accessibility for mercury increases as the pore size decreases, and is close to 100% for pores with a throat radius smaller than ~5 nm (50 Å; Fig. 9C). A similar inconsistency between results obtained using SANS, MICP and helium porosimetry was encountered in section 3.2.4 in relation to calculating total porosity, and it was generally attributed to different specific properties of nanostructural probes used by invasive and non-invasive methods of measurement (size, surface affinity and mechanical effect on the rock matrix). The dramatic discrepancy between the pressurised mercury-based and methane-based results (Fig. 9B and 9C) points to the specifics of pore penetration mechanisms for the two fluids: individual molecules of supercritical methane adsorb on the rock-pore interface and then fill the pore space starting from the smallest nanopores in the organic matrix (capillary condensation), whereas mercury remains in a continuous phase and is progresively forced through the gradually decreasing pore throats as a non-wetting liquid. The Hg entry pressure for throats of size roughly corresponding to capillary condensation (<10 nm in diameter) in the samples studied is very large - ~1240 bar (18,000 psia). It is well accepted that small nanopores in shales are hosted by relatively soft organic matter (kerogen) (e.g., Chalmers and Bustin, 2006; Strapoc et al., 2010; Kuila and Prasad, 2011; Milliken et al., 2013). In addition it has been shown that methane can penetrate the kerogen and slightly alter its structure at pressures just above ~200 bar (Neil et al., 2020b and section 3.2.3 in this work).

(A)

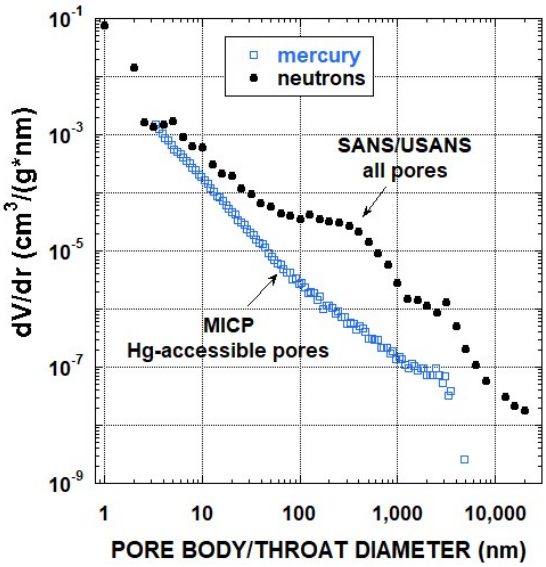

(B) (C)

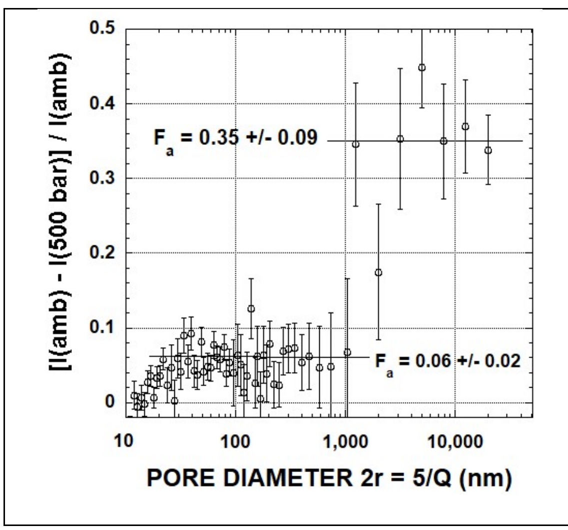

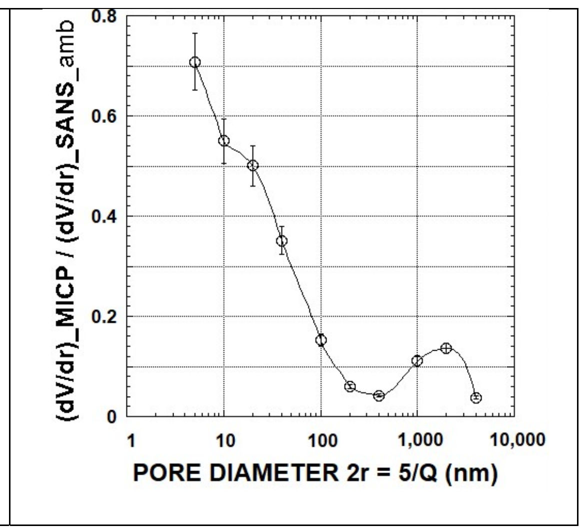

Figure 9. (A) Comparison of the dV/dr_b results for all pores plotted versus pore body diameter, 2r=5/Q (based on SANS/USANS data, black circles) with the dV/dr_t results for mercury-accessible pores plotted versus pore throat radius, r_t (based on MICP data, open blue squares). (B) Fraction of accessible pores calculated from SANS/USANS results. (C): Fraction of accessible pores calculated from MICP and ambient SANS/USANS results.

On the other hand, the micro-architecture of the total pore space (accessible plus inaccessible) measured at ambient conditions using SANS/USANS is not deformed by external forces. Therefore, we conclude that there is a high likelihood that mercury is forced into the small mesopores at pressures over 1000 bar and breaks through the interpore structural barriers, penetrates the originally inaccessible nanopores and, consequently, alters the nanostructure of shale. This finding supports previous suggestions that mercury at high pressure may cause artifacts in porosity determination (Bustin et al., 2008; Kuila and Prasad, 2011; Mastalerz et al., 2013). This hypothesis requires further investigation given its potential practical consequences. It also highlights the unique place of the non-invasive methods of SANS (and SAXS) in the toolbox of energy materials research.

5. Conclusions

A contrast-matching SANS and USANS study of Marcellus shale core of dry gas window maturity exhumed from the depth of 2159 m (7084 feet) revealed the following:

(1) Pores are statistically anisotropic and the degree of anisotropy depends on the pore size. Specifically, for pore diameters ~2.5 to 250 nm, anisotropy is smaller (the SANS/USANS iso-size ratio $\mathscr{R} = 0.38$) than for pores ~500 nm to 6 μm in diameter ($\mathscr{R} = 0.49$). Pore anisotropy is an important parameter for shale gas reservoirs because it results in different pore accessibility in various directions and impacts gas diffusion and fluid transport behavior. In addition, evaluation of the true porosity is important for porosimetric techniques that assume spherical pore shape; a correction factor may need to be developed to account for the error introduced by this assumption.

(2) SANS/USANS-determined total apparent porosity (open plus closed pores) of fractal-like pores with diameter ≥ 2 nm is about 6%, but porosity accessible to methane is only about 0.5%. For comparison, MICP and helium accessible porosity were determined to be 1.68% and 6.88%, respectively. Porosity of the additional (non-fractal) population of pores with diameter < 2 nm lies in the interval 1% to 5.9%, determined from He-porosimetry and MICP results, thus indicating that most of the pore volume is contained in micropores, in agreement with other studies on Marcellus shale.

(3) Methane introduced to macropores and large mesopores does not change its density. However, for pore diameters < 25 nm methane strongly condenses in confinement. In addition, exposure to methane at $p = 500$ bar leads to the formation of additional (excess) clusters of condensed CD_4 with diameters centered at about 5.5 nm. This densification of methane in small nanopores and the formation of large-density nano-clusters are likely reasons for difficulty in liberating methane during production and, consequently, low methane recovery rates.

(4) The pore-size dependence of differential pore volume, dV/dr, determined using the non-invasive method of SANS/USANS is fundamentally inconsistent with MICP results, which leads us to a working hypothesis that invasion of mercury at pressures over 1000 bar dramatically alters the structure of the meso- and micropores in shale. This hypothesis needs to be tested, because, if confirmed, it may have important implications for interpretations of MICP data.

Acknowledgements

This material is based upon work supported by the U.S. Department of Energy, Office of Science, Office of Basic Energy Sciences, Chemical Sciences, Geosciences, and Biosciences Division under Award Number DE-SC0006978. This work was supported by the Australian Nuclear Science and Technology Organisation in providing the SANS and USANS neutron research facilities used in this work. Additional support was provided by the Australian Research Council Grants LE200100209 and DP200102517.

Appendix is attached as a separate file.

References

Anitas, M.E., 2017. Small-Angle Scattering from Mass and Surface Fractals, Complexity in Biological and Physical Systems - Bifurcations, Solitons and Fractals. Ricardo López-Ruiz (Editor), IntechOpen, DOI: 10.5772/intechopen.70870. Available from: https://www.intechopen.com/chapters/57485

Anovitz, L.M., Cole, D.R., 2015. Characterization and analysis of porosity and pore structures. Reviews in Mineralogy and Geochemistry 80, 61-164.

Bahadur, J., Radlinski, A.P., Melnichenko, Y.B., Mastalerz, M., Schimmelmann, A., 2015. Small-angle and Ultrasmall-angle neutron scattering (SANS/USANS) study of the New Albany Shale: A treatise on microporosity, Energy & Fuels 29, 567-576.

Bahadur, J, Medina, C.R., He, L., Melnichenko, J.B., Rupp, J.A., Blach, T.P., Mildner, D.F.R., 2016. Determination of closed porosity in rocks by small-angle neutron scattering. Journal of Applied Crystallography 49, 2021-2030.

Bahadur, J., Ruppert, L.F., Pipich, V., Sakurovs, R., Melnichenko,Y.B., 2018. Porosity of the Marcellus shale: A contrast matching small-angle neutron scattering study. International Journal of Coal Geology 188, 156-164.

Baker, R.W., 2012. Membrane Technology and Applications. Third Edition. Table A15, p.567. John Wiley & Sons, Ltd.

Benmouna, M., Hammouda, B., 1997. The zero average contrast condition: Theoretical predictions and experimental examples. Progress in Polymer Science 22 (1), 49-92.

Blach, T.P., Radlinski, A.P., Edwards, D.S., Boreham, C., Gilbert, E.P., 2020. Pore anisotropy in unconventional hydrocarbon source rocks: A small-angle neutron scattering (SANS) study on the Arthur Creek Formation, Georgina Basin, Australia. International Journal of Coal Geology 225, 103495, doi:10.1016/j.coal.2020.103495

Blach, T., Radlinski, A.P., Edwards, D.S., Boreham, C., Rehm, C., de Campo, L., Gilbert, E.P., 2018. Fingerprint of hydrocarbon generation in the southern Georgina Basin, Australia, revealed by small angle neutron scattering. International Journal of Coal Geology 186, 135-144.

Broseta, D., Barre, L., Vizika, O., 2001. Capillary condensation in fractal porous medium. Physical Review Letters 86, 5313-5316.

Bustin, R. M., Bustin, A.M.M., Cui, X., Ross, D.J.K., Murthy Pathi, V.S., 2008. Impact of shale properties on pore structure and storage characteristics: SPE Paper No 119892, presented at the SPE Shale Gas Production Conference, Society of Petroleum Engineers, Fort Worth, USA, 16-18 November, 2008, doi: 10.2118/119892-MS

Cao, P., Liu, J., Leong, Y-W., 2017. A multiscale-multiphase simulation model of the evaluation of shale gas recovery coupled the effect of water flowback. Fuel 199, 191-205. https://doi.org/10.1016/j.fuel.2017.02.078

Chalmers, G. R. L., Bustin, R.M., 2006, The organic matter distribution and methane capacity of the Lower Cretaceous strata of Northeastern British Columbia, Canada. International Journal of Coal Geology 70, 223–239, doi: 10.1016/j.coal.2006.05.001.

Chalmers, G.R., Bustin, R.M., Power, I.M., 2012. Characterization of gas shale pore systems by porosimetry, pycnometry, surface area, and field emission scanning electron microscopy/transmission electron microscopy image analyses: Examples from the Barnett, Woodford, Haynesville, Marcellus, and Doig units. AAPG Bull. 96 (6), 1099-1119.

Cherfallot, G.J., Levitz, P.E., Michel, P., Kohler, E., Jestin, J., Barré, L., 2020. Probing Multiscale Structure of Mineral and Nanoporous Kerogen Phase in Organic-Rich Source Rocks: Quantitative Comparison of Small-Angle X-ray and Neutron Scattering. Energy & Fuels 34 (8), 9339-9354, https://doi.org/10.1021/acs.energyfuels.0c01146

Chiang, W.-S., Georgi, D., Yildrim, T., Chen, J.-H., Liu, Y, 2018. A non-invasive method to directly quantify surface heterogeneity of porous materials. Nature Communications (2018)9:784; doi: 10.1038/s41467-018-03151-w

Clarkson, C. R., Solano, N., Bustin, R.M., Bustin,A.M.M., Chalmers, G.R.L., He, L., Melnichenko, Y.B., Radliński, A.P., Blach, T.P., 2013. Pore structure characterization of North American shale gas reservoirs using USANS/SANS, gas adsorption, and mercury intrusion: Fuel 103, 606-616, doi: 10.2118/j.fuel.2012.06.119.

Debye, P., Anderson, H.R., Brumberger, R., 1957. Scattering by an inhomogeneous solid. II. The correlation function and its application. Journal of Applied Physics 28, 679-683.

Dong, Z., Holditch, S., McVay, D., 2013. Resource evaluation for shale gas reservoirs. SPE Econ. Manag. 5, 5-16. https://doi.org/10.2118/152066-PA

Eberle, A.P.R., King H.E., Ravikovitch, P.I., Walters C.C, Rother, G., Wesolowski, D.J., 2016. Direct measure of the dense methane phase in gas shale organic porosity by neutron scattering. Eneegy & Fuels 30, 9022-9027.

Elsaig, M., Aminian. K., Ameri, S., Zamirian, M., 2016. Accurate evaluation of Marcellus Shale petrophysical properties. SPE-184042-MS. https://doi.org/10.2118/184042-MS

Espinat, D., 1990. Application des techniques de diffusion de la lumière, des rayons X et des neutrons à l'étude des systèmes colloïdaux. Revue de l'Institut Français du Pétrole 45 (6), 131 pp, Éditions Technip.

Fan, E., Tang, S.,Zhang, C., Guo, Q., Sun, C., 2014. Methane sortption capacity of organics and clays in high-over matured shale-gas systems.

Faucher, S., Aluru, N., Bazant, M.Z., Blankschtein, D., Brozena, A.H., Cumings, J., Pedro de Sousa, J., Elimelech, M., Epsztein, R., Fourkas, J.T., Rajan, A.G., Kulik, H.J., Levy, A., Majumdar, A., Martin, C., McEldrew, M., Misra, R.P., Noy, A., Pham, T.A., Reed, M., Schwegler, E., Siwy, Z., Wang, Y-H., Strano, M., 2019. Critical knowledge gaps in mass transport through single digit nanopores: a review and perspective. Journal of Physical Chemistry C 123, 21309-21326.

Ghanizadeh, A., S. Bhowmik, O.H. Ardakani, H. Sanei, and C.R. Clarkson, 2015a, A comparison of shale permeability coefficients derived using multiple non-steady-state measurements techniques: Examples from the Duvernay Formation, Alberta (Canada): Fuel, v. 140, p. 371−387, doi: 10.1016/j.fuel.2014.09.073.

Gilbert, E.P., Auvray, L., Lal, J, 2001. Structure of polyelectrolyte chains confined in nanoporous glass. Macromolecules 34, 4942-4948.

Gregg, S. J., Sing, K. S. W., 1982. Adsorption, Surface Area and Porosity. Second edition. Academic Press, New York.

Gu, X., Cole, D.R., Rother, G., Mildner, D.F.R., Brantley, S., 2015. Pores in Marcellus shale: A neutron scattering and FIB-SEM study. Energy and Fuels 29 (3), 1295-1308.

Gu, X., Mildner, D.F.R., Ultra-small-angle neutron scattering with azimuthal asymmetry. Journal of Applied Crystallography 49, 934-943 (2016).

Gu, X., Mildner, D.F.R., 2018. Determination of porosity in anisotropic fractal systems by neutron scattering.Journal of Applied Crystallography 51, 175-184.

Hall, P.L., Mildner, D.F.R. 1983. On the analysis of small-angle scattering with azimuthal symmetry. Journal of Applied Physics 54(1), 427-428.

He, L., Melnichenko, Y.B., Mastalerz, M., Sakurovs, R., Radlinski, A.P., Blach,T., 2012. Pore accessibility by methane and carbon dioxide in coal as determined by neutron scattering. Energy & Fuels 26, 1975-1983.

Hinde, A.L., 2004. PRINSAS - a Windows-based computer program for the processing and interpretation of small-angle scattering data tailored to the analysis of sedimentary rocks. Journal of Applied Crystallography 37, 1020-1024.

Ilavsky, J., Jemian, P.R., 2009. Irena: tool suite for modeling and analysis of small-angle scattering, Journal of Applied Crystallography 42, 347-353.

Jubb, A.M., Ruppert, L.F., Youngs, T.G.A., Headen, T.F., 2020. Exploring methane behavior in Marcellus Shale micropores via contrast matching neutron scattering. Energy & Fuels 34, 10926-10932.

Jarvie, D.M., Hill, R.J., Ruble, T.E., Pollastro, R.M., 2007. Unconventional shale-gas systems: The Mississippian Barnett Shale of north-central Texas as one model for thermogenic shale-gas assessment. AAPG Bulletin 91, 475-499.

Jensen, G.V., Barker, J.G., 2018. Effects of multiple scattering encountered for various small-angle scattering model functions. Journal of Applied Crystalography 51, 1455-1466.

Katz, A. J., Thompson, H.M., 1986. Quantitative prediction of permeability in porous rock. Physical Review B 34, 11, 8179.

Kuila, U., Prasad, M., 2011. Surface area and pore-size distribution in clays and shales: SPE Paper No 146869, presented at the SPE Annual Technical Conference and Exhibition, Denver, USA, 30 Oct – 2 Nov, 2011. http://www.spe.org/atce/2011/pages/schedule/tech_program/documents/spe146869%201.pdf

Lee, D.S., Herman, J.D., Elsworth, D., Kim, H.T., Lee, H.S., 2011. A critical evaluation of unconventional gas recovery from the Marcellus Shale, Northeastern United States. KSCE Journal of Civil Engineering 15, 679-687. DOI 10.1007/s12205-011-0008-4

Li, Y.-H., Lu, G.O., Rudolph, V., 1999. Compressibility and fractal dimension of fine coal particles in relation to pore structure characterisation using mercury porosimetry. Paricles & Particle Systems Characterization 16, 25-31.

Li, Y., Song, D., Liu, S., Ji, G., Hao, H., 2021. Evaluation of pore properties in coal through compressibility correction based on mercury intrusion porosimetry: a practical approach. Fuel 291 (1), https://doi.org/10.1016/j.fuel.2021.120130

Lijun, Y., Yili, K., Qiang, C., Chaohe, F., Pengfei, Y., 2017. Prospect of shale gas recovery enhancement by oxidation-induced rock burst. Natural Gas Industry B 4, 449-456.

Liu, S., Zhang, R., 2020. Anisotropic pore structure if shale and gas injection-induced nanopore alternation: A small angle neutron scattering study. International Journal of Coal Geology 219, https://doi.org/10.1016/j.coal.2020.103384.

Luffel, D.L., C.W. Hopkins, and P.D. Shettler, 1993, Matrix permeability measurements of gas productive shales: SPE Annual Technical Conference and Exhibition, Houston, Texas, October 3–6, 1993, SPE-26633-MS, 10 p., doi: 10.2118/26633-MS.

Mastalerz, M., Hampton, L., Drobniak, A., Loope, H., 2017. Significance of analytical particle size in low-pressure N_2 and CO_2 adsorption of coal and shale. International Journal of Coal Geology 178, 122-131.

Mastalerz, M., Drobniak, A., Hower J.C., 2021. Controls on reservoir properties in organic-matter-rich shales: Insights from MICP analysis. Journal of Petroleum Science and Engineering 196, 107775, https://doi.org/10.1016/j.petrol.2020.107775

Mastalerz, M., Schimmelmann, A., Drobniak, A., Chen, Y., 2013. Porosity of Devonian/Mississippian New Albany Shale across a maturation gradient – Insights from organic petrology, gas adsorption, and mercury intrusion. AAPG Bulletin 97, 10, 1621-1643. http://dx.doi.org/10.1306/04011312194

Melnichenko, Y.B., He, L., Sakurovs, R., Kholodenko, A.L., Blach, T., Mastalerz, M., Radlinski, A.P., Cheng, G., Mildner, D.F.R., 2012. Accessibility of pores in coal to methane and carbon dioxide. Fuel 91, 200-208.

Melnichenko, Y.B., 2016. Small-Angle Scattering from Confined and Interfacial Fluids. Applications to Energy Storage and Environmental Science. Springer International Publishing, Cham, 314 pp.

Milliken, K. L., Rudnicki, M., Awwiller, D.A., Zhang, T., 2013, Organic matter-hosted pore system, Marcellus Formation (Devonian), Pennsylvania. AAPG Bulletin 97, 177-200. doi: 10.1306/07231212048.

Neil, C. Hjelm, R.P., Hawley, M.E., Watkins, E.B., Cockreham, C., Wu, D., Mao, Y., Fischer, T.B., Stokes, M.R., Xu, H., 2020a. Small-angle neutron scattering (SANS) characterization of clay-and carbonate-rich shale at elevated pressures. Energy Fuels. 34, 8178–8185.

Neil, C.W., Mehana, M., Hjelm, R.P., Hawley, M.E., Watkins, E.B., Mao, Y., Viswanathan, H., Kang, Q., Xu,H., 2020b. Reduced methane recovery at high pressure due to methane trapping in shale nanopores. Communications Earth & Environment, 1-49; https://doi.org/10.1038/s43247-020-00047-w

NIST calculator of SLD: https://www.ncnr.nist.gov/resources/sldcalc.html

Peacesoftware methane density data: http://peacesoftware.de/einigewerte/methan_e.html

Pfeifer, P., Avnir, D., 1983. Chemistry in noninteger dimensions between two and three. I. Fractal theory of heterogeneous surfaces. Journal of Chemical Physics 79, 3558 -3565.

Radlinski, A.P., Boreham, C.J., Wignall,G.D., Lin, J.-S., 1996. Microstructural evolution of source rocks during hydrocarbon generation: a small angle scattering study. Physical Review B1, 53(21), 14152-14160.

Radlinski, A.P., Radlinska, E.Z., 1999. The microstructure of pore space in coals of different rank: a small angle scattering and SEM study. In: M. Mastalerz, M. Glikson, S.D. Golding (Eds), Coalbed Methane: Scientific, Environmental and Economic Evaluation), Kluwer Academic Publishers, Dodrecht, 329-365.

Radlinski, A.P., Boreham, C.J., Lindner, P., Randl, O.G., Hinde, A.L., Hope, J.M., 2000. Small angle neutron scattering signature of oil generation in artificially and naturally matured hydrocarbon source rocks. Organic Geochemistry 31, 1–14.

Radlinski, A.P., Ioannidis, M.A., Hinde, A.L., Hainbuchner, M., Baron, M., Rauch, H., Kline, S.R., 2004a. Angstrom-to-millimeter characterization of sedimentary rock microstructure. Journal of Colloid and Interface Science 274 (2), 607-612.

Radlinski, A.P., Mastalerz, M., Hinde, A.L., Hainbuchner, M., Rauch, H., Baron, M., Lin,J.S., Fan, L., Thiyagarajan,P., 2004b. Application of SAXS and SANS in evaluation of porosity, pore size distribution and surface area of coal. International Journal of Coal Geology 59, 245-271.

Radlinski, A.P., Kennard, J.M., Edwards, D.S., Hinde, A.L., Davenport, R., 2004c. Hydrocarbon generation and expulsion from Early Cretaceous source rocks in the Browse Basin, North West Shelf, Australia: a small angle neutron scattering study. Australian Petroleum Production and Exploration Association Journal, 151-180.

Radlinski, A.P., 2006. Small Angle Neutron Scattering and the Microstructure of Rocks. In: Wenk H.-R., editor. Neutron Scattering in Earth Sciences, Reviews in Mineralogy and Geochemistry 63, 363-397.

Radlinski, A.P., Busbridge, T.L., MacA Gray, A., Blach, T.P., Cheng, G., Melnichenko, Y.B., Cookson, D.J., Mastalerz, M., Esterle, J., 2009a. Dynamic micromapping of CO_2 sorption in coal, Langmuir 25(4), 2385-2389.

Radlinski, A.P., Congo, T.L., MacA. Gray, A., Blach, T.P., Cookson, D.J., 2009b. Small angle X-ray scattering mapping and kinetics study of sub-critical CO_2 sorption by two Australian coals, International Journal of Coal Geology 77(1), 80-89.

Rehm, C., Brûle, A., Freund, A.K. and Kennedy, S.J., 2013. Kookaburra: the ultra-small-angle neutron scattering instrument at OPAL", Journal of Applied Crystallography 46, 1699–1704.

Rouquerol, F., Rouquerol, J., Sing, K.S.W., Llewellyn, P., Maurin, G., 2014. Adsorption by Powders and Porous Solids: Principles, Methodology and Applications, 2^{nd} edition. Academic Press, Oxford, UK, 630 pp.

Ruppert, L., Sakurovs, R., Melnichenko, Y.B., Blach, T.P., He, L., Mildner, D.F.R., 2013. A USANS/SANS study of the accessibility of pores in the Barnett shale to methane and water., Energy & Fuels. 27, 772-779. 10.1021/ef301859s.

Schmidt, P.W., 1982. Interpretation of small angle scattering curves proportional to a negative poper of the scattering vector. Journal of Applied Crystallography 15, 567-569.Sigal, R. F., 2009. A methodology for blank and conformance corrections for high pressure mercury porosimetry. Measurement Science and Technology 20, 045108.

Sokolova, A., A.E. Whitten, L. de Campo, J. Christoforidis, A. Eltobaji, J. Barnes, F. Darmann and A. Berry, 2019, "Performance and characteristics of the BILBY time-of-flight small-angle neutron scattering instrument", Journal of Applied Crystallography 52, 1-12.

Strąpoć, D., Mastalerz, M., Schimmelmann, A., Drobniak, A., Hasenmueller, N.R., 2010. Geochemical constraints on the origin and volume of gas in the New Albany Shale (Devonian-Mississippian), eastern Illinois Basin. AAPG Bulletin 94, 1713–1740, doi: 10.1306/06301009197.

Thomas, JJ., Valenza J.J., II, Craddock, P.R., Bake, K.D., Pomerantz, A.E., 2014. The neutron scattering length density of kerogen and coal as determined by CH_3OH/CD_3OH exchange. Fuel 117, 801-808.

Unitrove methane density data : https://www.unitrove.com/engineering/tools/gas/natural-gas-density

US Energy Information Administration, Annual Energy Outlook 2019 with projections to 2050.

Usoltseva, N.V., Korobochkin, V.V., Balmashnov, M.A., Dolinina, A.S., 2014. Characterization of copper and aluminum AC electrochemical oxidation products. Procedia Chemistry 10, 320-325.

Vineyard, G.H., 1954. Multiple Scattering of Neutrons. Physical Review 96, 93–98.

Wang, Y., Qin, Y., Zhang, R., He, L., Anovitz, L.M., Bleuel, M., Mildner, D.F.R., Liu, S., Zhu, Y. 2018. Evaluation of nanoscale accessible pore structures for improved prediction of gas production potential in Chinese marine shales. Energy Fuels 32, 12447-12461.

Wang, Y., Zhu, Y., Zhang, R., Anovitz, L.M., Bleuel, M., Liu, S., Chen, S., 2020. SANS coupled with fluid invasion approaches for characterization of overall nanopore structure and mesopore connectivity of organic-rich marine shales in China. International Journal of Coal Geology 217, https/doi.org/10.1016/j.coal.2019.103343.

Wong, P-z., Lin, J-s., 1988. Studying fractal geometry on submicron length scales by small-angle scattering. Mathematical Geology 20(6), 655-665.

Wood, K., Mata, J.P., Garvey, C.J., Wu, C.-M. Hamilton, W.A., Abbeywick, P., Bartlett, D., Bartsch, F., Baxter, P., Booth, N., Brown, W., Christoforidis, J., Clowes, D., d'Adam, T., Darmann, F., Deura, M., Harrison,S., Hauser, N., Horton, D., Federici, D., Franceschini, F., Hanson, H., Imamovic, E., Imperia, P., Jones, M., Kennedy, S., Kim, S., Lam, T., Lee, W.T., Lesha, M., Mannicke, D., Noakes, T., Olsen, S.R., Osborn, J.C., Penny, D., Perry, M., Pullen, S.A., Robinson, R.A., Schulz, J.C., Xiong N., Gilbert, E.P., 2018. QUOKKA, the pinhole small-angle neutron scattering instrument at the OPAL research reactor, Australia: design, performance, operation and scientific highlights. Journal of Applied Crystallography 51, 294-314.

Zhang, J., G. Cheng, 2021. Technical aspects of the pore structure in shales measured by small-angle and ultrasmall-angle neutron scattering: A mini review. Energy&Fuels 35, 1957-1965.

Zhang, R., Liu, S., 2021. Nanoscale coal deformation and alteration of porosity and pore orientation under uniaxial compression: An in-situ SANS study. Rock Mechanics and Rock Engineering, https://doi.org/10.1007/s00603-020-02321-x

Zhang, R., Liu, S., He, L., Blach, T.P., Wang, Y., 2020. Characterizing anisotropic pore structure and its impact on gas storage and transport in coalbed methane and shale gas reservoirs. Energy Fuels 34, 3161-3172.